

High-order finite-difference entropy stable schemes for two-fluid relativistic plasma flow equations

Deepak Bhoriya[†], Harish Kumar[†], and Praveen Chandrashekar[‡]

[†]Department of Mathematics, Indian Institute of Technology Delhi, New Delhi, India

[‡]Centre for Applicable Mathematics, Tata Institute of Fundamental Research,
Bangalore, India

Contents

1	Introduction	2
2	Two-fluid relativistic plasma flow equations	3
3	Analysis of continuous problem	5
4	Semi-discrete entropy stable schemes	7
4.1	Entropy stable numerical schemes for the fluid equations	7
4.1.1	High-order entropy conservative schemes for fluid equations	7
4.1.2	High-order entropy stable schemes for fluid equations	10
4.2	Discretization of Maxwell's equations	12
5	Fully discrete scheme	12
5.1	Explicit schemes	12
5.2	ARK-IMEX schemes	13
5.2.1	Second order time discretization.	13
5.2.2	Third and fourth-order time discretization.	14
6	Numerical results	14
6.1	One-dimensional test cases	15
6.1.1	Accuracy test	15
6.1.2	Relativistic Brio–Wu test problem with finite plasma skin depth	16
6.1.3	Self-similar current sheet with finite resistivity	20
6.2	Two-dimensional test cases	20
6.2.1	Relativistic Orzag-Tang test case	21
6.2.2	Relativistic two-fluid blast problem	21
6.2.3	Relativistic two-fluid GEM challenge problem	30
7	Conclusion	32
A	Proof of Proposition 3.1	39

arXiv:2210.08568v2 [math.NA] 10 May 2023

B	Barth scaling of right eigenvectors	40
B.1	Right eigenvectors	41
B.2	Barth scaling and entropy scaled right eigenvectors	42
C	ARK3-IMEX coefficients table	44

Abstract

In this article, we propose high-order finite-difference entropy stable schemes for the two-fluid relativistic plasma flow equations. This is achieved by exploiting the structure of the equations, which consists of three independent flux components. The first two components describe the ion and electron flows, which are modeled using the relativistic hydrodynamics equation and the third component is Maxwell's equations. The coupling of the ion and electron flows and electromagnetic fields is via source terms only, but the source terms do not affect the entropy evolution. To design semi-discrete entropy stable schemes, we extend the entropy stable schemes for relativistic hydrodynamics in [1] to three dimensions. This is then coupled with entropy stable discretization of the Maxwell's equations. Finally, we use SSP-RK schemes to discretize in time. We also propose ARK-IMEX schemes to treat the stiff source terms; the resulting nonlinear set of algebraic equations is local (at each discretization point) and hence can be solved cheaply using the Newton's Method. The proposed schemes are then tested using various test problems to demonstrate their stability, accuracy and efficiency.

Keywords: Finite-difference entropy stable schemes, two-fluid relativistic plasma flows, balance laws, IMEX-schemes

1 Introduction

Relativistic plasma flows play a central role in astrophysics. In these flows, fluids moving with the speed comparable to the speed of light interact with electric and magnetic fields. Some examples are pulsar winds, gamma-ray bursts, relativistic jets from active galactic nuclei, and quasars [2], [3], [4], [5]. To model relativistic plasma flows, often, equations of relativistic Magneto-hydrodynamics (RMHD) are used [6], [7], [8], [9], [10], [11]. However, RMHD has limitations when modeling several astrophysical systems, like pulsar, gamma-ray burst, etc., see [12] for a detailed discussion. Following the development of non-relativistic two-fluid plasma flow equations [13], [14], [15], [16], [17], [18], [19], several authors have considered an analogous relativistic two-fluid plasma flow equations [20], [21], [22], [23], [24].

Two-fluid relativistic plasma flow equations describe each fluid (ion and electron) in plasma using the equations of special relativistic hydrodynamics (RHD). The fluid components are coupled via electromagnetic quantities using Lorentz force terms. Finally, the electric and magnetic fields are evolved using Maxwell's equations, where current and charges are described using fluid variables. The resulting set of PDEs is a Hyperbolic system of Balance laws with nonlinear flux and stiff source. Due to nonlinearity in the flux, the solutions will exhibit discontinuities [25]. Hence, we need to consider the weak solutions, which can be characterized using the Rankine-Hugoniot condition across the discontinuities. As the weak solutions are non-unique, entropy inequality is imposed to avoid nonphysical solutions. More recently, even the entropy solutions for the systems have been shown to be non-unique [26], still, entropy stability is one of the few nonlinear stability estimates for the solutions, and hence it is desirable to have a numerical scheme which replicates this stability at the discrete level.

As the flux and source terms are nonlinear, in general, it is not possible to find an analytical solution for the two-fluid relativistic plasma flow equations. Hence, the development of stable, efficient and accurate numerical methods is highly desirable. However, in addition to the well-known difficulties in designing stable numerical schemes for hyperbolic balance laws [27], [25], there are several additional challenges in designing such a scheme for two-fluid relativistic plasma flow equations. First, we need to compute the primitive variables from the conservative variables as the analytical expressions are not available. Second, we must satisfy additional constraints for the magnetic and electric fields. Third, we have nonlinear stiff source terms, and a suitable time implicit treatment of such source is highly desirable. Furthermore, as discussed above, it is also desirable to have entropy stability of the scheme.

30 Given these difficulties, there are few numerical methods for the two-fluid relativistic plasma flow
 31 model. In [28], authors have simulated the relativistic magnetic reconnection problem by assuming the
 32 symmetric motions of the fluid species, which was further improved in [20] to include the independent
 33 motion of the two-fluid species under a guide field. In [22], authors used one-dimensional two-fluid
 34 relativistic plasma flow system to investigate the importance of the electric-field-dominated regime in
 35 the dynamics of a strongly magnetized plasma by simulating a standing shock front. In [23], authors
 36 presented a third-order accurate explicit multidimensional numerical scheme for special relativistic two-
 37 fluid plasma flow equations. Here, the authors used the method of generalized Lagrange multiplier to
 38 keep the divergence error small. Divergence-free and constraint preserving multidimensional scheme has
 39 been designed in [12, 29].

40 In this article, we propose arbitrarily high-order finite-difference entropy stable schemes for the
 41 relativistic two-fluid plasma flow model. High order finite-difference entropy stable schemes for general
 42 hyperbolic systems were first proposed in [30, 31]. Recently, several authors have developed entropy stable
 43 finite-difference scheme for non-relativistic fluids and plasma flows [15], [32], [33], [34]. For the relativistic
 44 fluids, Duan *et.al* [35], Biswas [36], and Bhoriya *et.al* [1] have proposed entropy stable schemes.

45 We proceed as follows.

- 46 • We first present the entropy framework for the two-fluid relativistic plasma flow equations. We
 47 also prove that the source terms do not affect entropy evolution.
- 48 • To design entropy stable scheme, we exploit the structure of the flux. Similar to the case of [15], the
 49 flux consists of three independent blocks. For the fluid parts, we extend the entropy conservative
 50 schemes of [1] to include a three-dimensional velocity field for each fluid component. This is then
 51 coupled with a Rusanov’s solver based on higher-order Maxwell’s discretization. The resultant
 52 scheme is then shown to be entropy conservative.
- 53 • To make the scheme entropy stable, following [30], [15], [1], we design high-order diffusion operator,
 54 for each component. As the source does not affect entropy evolution, the semi-discrete scheme is
 55 then shown to be entropy stable.
- 56 • As the source terms are stiff, in addition to the explicit Runge-Kutta method, we also propose
 57 IMEX schemes for the model, where flux contributions are treated explicitly, and the source is
 58 treated implicitly. The resulting set of nonlinear algebraic equations is local in each cell and are
 59 solved using Newton’s method for nonlinear systems.

60 The rest of the article is organized as follows. In Section (2), we describe the two-fluid relativistic
 61 plasma flow equations. In Section (3), we discuss hyperbolicity and the entropy framework for the
 62 model. In Section (4), we propose semi-discrete entropy stable numerical schemes for the model. This
 63 includes the derivation of the fluid entropy conservative numerical flux and the construction of the high-
 64 order entropy diffusion operators. We also describe the discretization of the Maxwell’s equations. In
 65 Section (5), we present the fully discrete scheme using time explicit and IMEX schemes. In Section (6),
 66 we provide detailed numerical tests in one and two dimensions.

67 2 Two-fluid relativistic plasma flow equations

The two-fluid relativistic plasma flows consist of electrons and ions, whose flows are governed by the
 equations of special relativistic flows. The macroscopic variables for the fluid parts are density, fluid
 velocity and pressure, denoted by ρ_α , \mathbf{u}_α , and p_α , respectively with $\alpha \in \{i, e\}$. Here, the subscripts
 $\{i, e\}$ denote the variables corresponding to the ion and electron species. These are coupled to Maxwell’s

equations via source terms. The complete system is given as follows:

$$\frac{\partial(\rho_i\Gamma_i)}{\partial t} + \nabla \cdot (\rho_i\Gamma_i\mathbf{u}_i) = 0, \quad (1a)$$

$$\frac{\partial(\rho_i h_i \Gamma_i^2 \mathbf{u}_i)}{\partial t} + \nabla \cdot (\rho_i h_i \Gamma_i^2 \mathbf{u}_i \mathbf{u}_i^\top + p_i \mathbf{I}) = r_i \Gamma_i \rho_i (\mathbf{E} + \mathbf{u}_i \times \mathbf{B}), \quad (1b)$$

$$\frac{\partial \mathcal{E}_i}{\partial t} + \nabla \cdot ((\mathcal{E}_i + p_i) \mathbf{u}_i) = r_i \Gamma_i \rho_i (\mathbf{u}_i \cdot \mathbf{E}), \quad (1c)$$

$$\frac{\partial(\rho_e \Gamma_e)}{\partial t} + \nabla \cdot (\rho_e \Gamma_e \mathbf{u}_e) = 0, \quad (1d)$$

$$\frac{\partial(\rho_e h_e \Gamma_e^2 \mathbf{u}_e)}{\partial t} + \nabla \cdot (\rho_e h_e \Gamma_e^2 \mathbf{u}_e \mathbf{u}_e^\top + p_e \mathbf{I}) = r_e \Gamma_e \rho_e (\mathbf{E} + \mathbf{u}_e \times \mathbf{B}), \quad (1e)$$

$$\frac{\partial \mathcal{E}_e}{\partial t} + \nabla \cdot ((\mathcal{E}_e + p_e) \mathbf{u}_e) = r_e \Gamma_e \rho_e (\mathbf{u}_e \cdot \mathbf{E}), \quad (1f)$$

$$\frac{\partial \mathbf{B}}{\partial t} + \nabla \times \mathbf{E} + \kappa \nabla \psi = 0, \quad (1g)$$

$$\frac{\partial \mathbf{E}}{\partial t} - \nabla \times \mathbf{B} + \chi \nabla \phi = -\mathbf{j}, \quad (1h)$$

$$\frac{\partial \phi}{\partial t} + \chi \nabla \cdot \mathbf{E} = \chi \rho_c, \quad (1i)$$

$$\frac{\partial \psi}{\partial t} + \kappa \nabla \cdot \mathbf{B} = 0, \quad (1j)$$

where, $\mathcal{E}_\alpha = \rho_\alpha h_\alpha \Gamma_\alpha^2 - p_\alpha$ are the energy densities, h_α are the specific enthalpy, Γ_α are the Lorentz factors, given by $\Gamma_\alpha = \frac{1}{\sqrt{1 - \mathbf{u}_\alpha^2}}$, $\mathbf{B} = (B_x, B_y, B_z)$ is the magnetic field vector, and $\mathbf{E} = (E_x, E_y, E_z)$ is the electric field vector. We have assumed the speed of light to be unity. We use notations, q_α for the particle charge and m_α for the particle mass, while the charge to mass ratios are denoted by $r_\alpha = \frac{q_\alpha}{m_\alpha}$, $\alpha \in \{i, e\}$. The total charge density ρ_c and the current density vector $\mathbf{j} = (j_x, j_y, j_z)$ are given by

$$\rho_c = r_i \rho_i \Gamma_i + r_e \rho_e \Gamma_e, \quad \mathbf{j} = r_i \rho_i \Gamma_i \mathbf{u}_i + r_e \rho_e \Gamma_e \mathbf{u}_e.$$

The above system of equations is closed using the equation of state, $h_\alpha = h_\alpha(p_\alpha, \rho_\alpha)$, where we use the ideal equation of state for h_α , which is given by

$$h_\alpha = 1 + \frac{\gamma_\alpha}{\gamma_\alpha - 1} \frac{p_\alpha}{\rho_\alpha},$$

where, $\gamma_\alpha = c_{p_\alpha}/c_{v_\alpha}$ is the ratio of specific heats. Accordingly, the polytropic index n_α , and the sound speed $c_\alpha = c_{s_\alpha}$ can be written as

$$n_\alpha = k_\alpha - 1 \quad \text{and} \quad c_\alpha^2 = \frac{k_\alpha p_\alpha}{n_\alpha \rho_\alpha h_\alpha},$$

68 where $k_\alpha = \frac{\gamma_\alpha}{\gamma_\alpha - 1}$ are constants.

69 Equations (1a) and (1d) are mass conservation laws for ion and electrons. Similarly, Equations (1b)
70 and (1e) represent momentum balance, where source terms are due to Lorentz force acting on the fluid
71 due to the electromagnetic variables. The energy conservation equations for ion and electron fluids
72 are (1c) and (1f), respectively. Here, source terms are kinetic energy contributions due to electric and
73 magnetic fields.

74 To deal with the electromagnetic constraints $\nabla \cdot \mathbf{B} = 0$ and $\nabla \cdot \mathbf{E} = \rho_c$, in (1g)-(1j), we consider the
75 perfectly hyperbolic formulation of the Maxwell's equations [37]. Here, (1g) and (1h) are the evolution
76 equations for the magnetic and electric fields, respectively. Equations (1i) and (1j) are equations for the
77 correction potentials ϕ and χ , and χ and κ are penalizing speeds.

3 Analysis of continuous problem

Let us introduce the notations, $D_\alpha = \Gamma_\alpha \rho_\alpha$ and $\mathbf{M}_\alpha = (M_{x_\alpha}, M_{y_\alpha}, M_{z_\alpha}) = \rho_\alpha h_\alpha \Gamma_\alpha^2 \mathbf{u}_\alpha$ for $\alpha \in \{i, e\}$. The vector of conservative variables \mathbf{U} can be written as,

$$\mathbf{U} = (\mathbf{U}_i^\top, \mathbf{U}_e^\top, \mathbf{U}_m^\top)^\top,$$

where $\mathbf{U}_i = (D_i, \mathbf{M}_i, \mathcal{E}_i)^\top$ are ion fluid variables, $\mathbf{U}_e = (D_e, \mathbf{M}_e, \mathcal{E}_e)^\top$ are electron fluid variables, and $\mathbf{U}_m = (\mathbf{B}, \mathbf{E}, \phi, \psi)^\top$ are Maxwell's variables. In two dimensions, let us also denote x - and y -directional fluxes as \mathbf{f}^x and \mathbf{f}^y , respectively. From (1), expressions for the fluxes can be written as,

$$\mathbf{f}^x = \begin{pmatrix} \mathbf{f}_i^x(\mathbf{U}_i) \\ \mathbf{f}_e^x(\mathbf{U}_e) \\ \mathbf{f}_m^x(\mathbf{U}_m) \end{pmatrix} \quad \text{and} \quad \mathbf{f}^y = \begin{pmatrix} \mathbf{f}_i^y(\mathbf{U}_i) \\ \mathbf{f}_e^y(\mathbf{U}_e) \\ \mathbf{f}_m^y(\mathbf{U}_m) \end{pmatrix},$$

where

$$\mathbf{f}_\alpha^x = \begin{pmatrix} D_\alpha u_{x_\alpha} \\ M_{x_\alpha} u_{x_\alpha} + p_\alpha \\ M_{y_\alpha} u_{x_\alpha} \\ M_{z_\alpha} u_{x_\alpha} \\ M_{x_\alpha} \end{pmatrix}, \quad \mathbf{f}_\alpha^y = \begin{pmatrix} D_\alpha u_{y_\alpha} \\ M_{x_\alpha} u_{y_\alpha} \\ M_{y_\alpha} u_{y_\alpha} + p_\alpha \\ M_{z_\alpha} u_{y_\alpha} \\ M_{y_\alpha} \end{pmatrix}, \quad \mathbf{f}_m^x = \begin{pmatrix} \kappa \psi \\ -E_z \\ E_y \\ \chi \phi \\ B_z \\ -B_y \\ \chi E_x \\ \kappa B_x \end{pmatrix}, \quad \mathbf{f}_m^y = \begin{pmatrix} E_z \\ \kappa \psi \\ -E_x \\ -B_z \\ \chi \phi \\ B_x \\ \chi E_y \\ \kappa B_y \end{pmatrix} \quad (2)$$

We note that the flux for the whole system contains three independent parts, two fluid parts modeled using the equations of special relativistic flows, and the third part is linear Maxwell's flux. These three parts are coupled via source terms, which are given as,

$$\mathbf{s} = \begin{pmatrix} \mathbf{s}_i(\mathbf{U}_i, \mathbf{U}_m) \\ \mathbf{s}_e(\mathbf{U}_e, \mathbf{U}_m) \\ \mathbf{s}_m(\mathbf{U}_i, \mathbf{U}_e) \end{pmatrix},$$

where,

$$\mathbf{s}_\alpha = \begin{pmatrix} 0 \\ r_\alpha D_\alpha (E_x + u_{y_\alpha} B_z - u_{z_\alpha} B_y) \\ r_\alpha D_\alpha (E_y + u_{z_\alpha} B_x - u_{x_\alpha} B_z) \\ r_\alpha D_\alpha (E_z + u_{x_\alpha} B_y - u_{y_\alpha} B_x) \\ r_\alpha D_\alpha (u_{x_\alpha} E_x + u_{y_\alpha} E_y + u_{z_\alpha} E_z) \end{pmatrix} \quad \text{and} \quad \mathbf{s}_m = \begin{pmatrix} 0 \\ 0 \\ 0 \\ -j_x \\ -j_y \\ -j_z \\ \chi \rho_c \\ 0 \end{pmatrix},$$

for $\alpha \in \{i, e\}$. Using the above notations, the system (1), for the two-dimensional case can be written in the conservation form as follows:

$$\frac{\partial \mathbf{U}}{\partial t} + \frac{\partial \mathbf{f}^x}{\partial x} + \frac{\partial \mathbf{f}^y}{\partial y} = \mathbf{s}. \quad (3)$$

Let us also introduce the vector of primitive variables $\mathbf{W} = (\mathbf{W}_i^\top, \mathbf{W}_e^\top, \mathbf{W}_m^\top)^\top$, where $\mathbf{W}_\alpha = (\rho_\alpha, \mathbf{u}_\alpha, p_\alpha)^\top$ and $\mathbf{W}_m = (\mathbf{B}, \mathbf{E}, \phi, \psi)^\top$. We follow the procedure given in [1, 38] to extract the primitive variables from the conservative variables. We define the set of admissible solution space

$$\Omega = \{\mathbf{U} \in \mathbb{R}^{18} : \rho_i > 0, \rho_e > 0, p_i > 0, p_e > 0, |\mathbf{u}_i| < 1, |\mathbf{u}_e| < 1\}.$$

The eigenvalues of the system in x -direction are,

$$\Lambda^x = \left\{ \frac{(1 - c_i^2)u_{x_i} - (c_i/\Gamma_i)\sqrt{Q_i^x}}{1 - c_i^2|\mathbf{u}_i|^2}, u_{x_i}, u_{x_i}, u_{x_i}, \frac{(1 - c_i^2)u_{x_i} + (c_i/\Gamma_i)\sqrt{Q_i^x}}{1 - c_i^2|\mathbf{u}_i|^2}, \right. \\ \left. \frac{(1 - c_e^2)u_{x_e} - (c_e/\Gamma_e)\sqrt{Q_e^x}}{1 - c_e^2|\mathbf{u}_e|^2}, u_{x_e}, u_{x_e}, u_{x_e}, \frac{(1 - c_e^2)u_{x_e} + (c_e/\Gamma_e)\sqrt{Q_e^x}}{1 - c_e^2|\mathbf{u}_e|^2}, \right. \\ \left. -\chi, -\kappa, -1, -1, 1, 1, \kappa, \chi \right\},$$

79 where, $Q_\alpha^x = 1 - u_{x_\alpha}^2 - c_\alpha^2(u_{y_\alpha}^2 + u_{z_\alpha}^2)$, $\alpha \in \{i, e\}$. For $\mathbf{U} \in \Omega$ and $\gamma_\alpha \in (1, 2]$ we have $c_\alpha < 1$ which
80 implies that $Q_\alpha^x > 0$, hence all the eigenvalues are real. The complete set of right eigenvectors for the
81 Jacobian matrix $\frac{\partial \mathbf{f}^x}{\partial \mathbf{U}}$ is given in Appendix (B.1). The Appendix also contains the eigenvalues and right
82 eigenvectors for the jacobian matrix $\frac{\partial \mathbf{f}^y}{\partial \mathbf{U}}$. Consequently, we can state the following Lemma.

83 **Lemma 3.1.** *The system (3) is hyperbolic for the states $\mathbf{U} \in \Omega$, with real eigenvalues and a complete*
84 *set of eigenvectors.*

We now introduce entropy functions for the two-fluid relativistic plasma flow equations. The entropy functions \mathcal{U}_α and associated entropy fluxes \mathcal{F}_α^d for the fluid part of the system (3) are given by,

$$\mathcal{U}_\alpha = -\frac{\rho_\alpha \Gamma_\alpha s_\alpha}{\gamma_\alpha - 1} \quad \text{and} \quad \mathcal{F}_\alpha^d = -\frac{\rho_\alpha \Gamma_\alpha s_\alpha u_{d_\alpha}}{\gamma_\alpha - 1}, \quad \alpha \in \{i, e\}, \quad d = x, y.$$

Here, $s_\alpha = \ln(p_\alpha \rho_\alpha^{-\gamma_\alpha})$. The pair $(\mathcal{U}_\alpha, \mathcal{F}_\alpha^d)$ is called an *entropy-entropy flux pair*. For simplicity, we only consider the one-dimensional case, i.e.,

$$\frac{\partial \mathbf{U}}{\partial t} + \frac{\partial \mathbf{f}^x}{\partial x} = \mathbf{s}. \quad (4)$$

85 The extension of entropy framework to higher dimensions is straightforward. We will now prove the
86 following result:

Proposition 3.1. *The smooth solutions of (4) satisfy the entropy equality,*

$$\partial_t s_\alpha + u_{x_\alpha} \partial_x s_\alpha = 0, \quad \alpha \in \{i, e\}.$$

As a consequence, every smooth function $H(s_\alpha)$ of s_α satisfies

$$\partial_t(\rho_\alpha \Gamma_\alpha H(s_\alpha)) + \partial_x(\rho_\alpha \Gamma_\alpha u_{x_\alpha} H(s_\alpha)) = 0. \quad (5)$$

In particular, we have the following entropy equality for the smooth solutions,

$$\partial_t \mathcal{U}_\alpha + \partial_x \mathcal{F}_\alpha^x = 0. \quad (6)$$

87 The proof is given in the Appendix (A).

Remark 3.1. *The entropy equality (6) in Proposition (3.1) is replaced by the entropy inequality*

$$\partial_t \mathcal{U}_\alpha + \partial_x \mathcal{F}_\alpha^x \leq 0, \quad (7)$$

88 *in the sense of distributions for non-smooth solutions.*

89 In the above analysis, we also note that the Maxwell's flux does not affect the fluid entropies. This
90 fact will be exploited to design semi-discrete high-order numerical schemes which will satisfy the entropy
91 inequality (7).

4 Semi-discrete entropy stable schemes

In this section, we will design semi-discrete entropy stable numerical schemes for the two-dimensional two-fluid relativistic plasma flow Eqns. (3). The extension to three dimensions is fairly easy. Let us consider the domain $D = I_x \times I_y$, where $I_x = (x_{min}, x_{max})$ and $I_y = (y_{min}, y_{max})$ which is discretized using a uniform mesh with cells of size $\Delta x \times \Delta y$. We define $x_i = x_{min} + i\Delta x$ for $0 \leq i \leq N_x$ and $y_j = y_{min} + j\Delta y$ for $0 \leq j \leq N_y$. The cell (i, j) is given by $I_{i,j} = [x_{i-1/2}, x_{i+1/2}] \times [y_{j-1/2}, y_{j+1/2}]$, where $x_{i+1/2} = \frac{x_i + x_{i+1}}{2}$ and $y_{j+1/2} = \frac{y_j + y_{j+1}}{2}$.

The semi-discrete finite difference scheme for the evolution of solution $\mathbf{U}_{i,j}$ at (x_i, y_j) of system (3) is given by,

$$\frac{d}{dt} \mathbf{U}_{i,j}(t) + \frac{1}{\Delta x} \left(\mathbf{F}_{i+\frac{1}{2},j}^x(t) - \mathbf{F}_{i-\frac{1}{2},j}^x(t) \right) + \frac{1}{\Delta y} \left(\mathbf{F}_{i,j+\frac{1}{2}}^y(t) - \mathbf{F}_{i,j-\frac{1}{2}}^y(t) \right) = \mathbf{s}(\mathbf{U}_{i,j}(t)), \quad (8)$$

where $\mathbf{F}_{i+\frac{1}{2},j}^x$, $\mathbf{F}_{i,j+\frac{1}{2}}^y$ are the numerical fluxes consistent with the continuous fluxes \mathbf{f}^x , \mathbf{f}^y , respectively.

4.1 Entropy stable numerical schemes for the fluid equations

To simplify the discussion, we will first present the discretization of the fluid part, i.e., we consider the following differential form:

$$\frac{\partial \mathbf{U}_\alpha}{\partial t} + \frac{\partial \mathbf{f}_\alpha^x}{\partial x} + \frac{\partial \mathbf{f}_\alpha^y}{\partial y} = \mathbf{s}_\alpha(\mathbf{U}_\alpha, \mathbf{U}_m), \quad (9)$$

for $\alpha \in \{i, e\}$. Let us now define:

Definition 4.1. *The numerical scheme*

$$\begin{aligned} \frac{d}{dt} \mathbf{U}_{\alpha,i,j}(t) + \frac{1}{\Delta x} \left(\mathbf{F}_{\alpha,i+\frac{1}{2},j}^x(t) - \mathbf{F}_{\alpha,i-\frac{1}{2},j}^x(t) \right) + \frac{1}{\Delta y} \left(\mathbf{F}_{\alpha,i,j+\frac{1}{2}}^y(t) - \mathbf{F}_{\alpha,i,j-\frac{1}{2}}^y(t) \right) \\ = \mathbf{s}_\alpha(\mathbf{U}_{\alpha,i,j}(t), \mathbf{U}_{m,i,j}(t)), \end{aligned} \quad (10)$$

is said to be entropy conservative if the following entropy equality is satisfied

$$\frac{d}{dt} \mathcal{U}_\alpha(\mathbf{U}_{ij}) + \frac{1}{\Delta x} \left(\hat{\mathcal{F}}_{\alpha,i+\frac{1}{2},j}^x - \hat{\mathcal{F}}_{\alpha,i-\frac{1}{2},j}^x \right) + \frac{1}{\Delta y} \left(\hat{\mathcal{F}}_{\alpha,i,j+\frac{1}{2}}^y - \hat{\mathcal{F}}_{\alpha,i,j-\frac{1}{2}}^y \right) = 0, \quad \alpha \in \{i, e\}, \quad (11)$$

where $\hat{\mathcal{F}}_{\alpha,i+\frac{1}{2},j}^x$, $\hat{\mathcal{F}}_{\alpha,i,j+\frac{1}{2}}^y$ are some numerical entropy flux functions consistent with the entropy fluxes \mathcal{F}_α^x , \mathcal{F}_α^y , respectively. Here $\mathbf{F}_{\alpha,i+\frac{1}{2},j}^x$, $\mathbf{F}_{\alpha,i,j+\frac{1}{2}}^y$ are the numerical fluxes consistent with \mathbf{f}^x , \mathbf{f}^y , respectively.

The scheme is said to be entropy stable if the following entropy inequality is satisfied:

$$\frac{d}{dt} \mathcal{U}_\alpha(\mathbf{U}_{\alpha,i,j}) + \frac{1}{\Delta x} \left(\hat{\mathcal{F}}_{\alpha,i+\frac{1}{2},j}^x - \hat{\mathcal{F}}_{\alpha,i-\frac{1}{2},j}^x \right) + \frac{1}{\Delta y} \left(\hat{\mathcal{F}}_{\alpha,i,j+\frac{1}{2}}^y - \hat{\mathcal{F}}_{\alpha,i,j-\frac{1}{2}}^y \right) \leq 0 \quad \alpha \in \{i, e\}, \quad (12)$$

To obtain the entropy stable schemes, we will first construct entropy conservative schemes and then add dissipative fluxes to obtain entropy inequality.

4.1.1 High-order entropy conservative schemes for fluid equations

Let us introduce *entropy variables*,

$$\mathbf{V}_\alpha(\mathbf{U}_\alpha) = \frac{\partial \mathcal{U}_\alpha}{\partial \mathbf{U}_\alpha}$$

and *entropy potentials*,

$$\psi_\alpha^x(\mathbf{U}_\alpha) = \mathbf{V}_\alpha^\top(\mathbf{U}_\alpha) \cdot \mathbf{f}_\alpha^x(\mathbf{U}_\alpha) - \mathcal{F}_\alpha^x(\mathbf{U}_\alpha), \quad \psi_\alpha^y(\mathbf{U}_\alpha) = \mathbf{V}_\alpha^\top(\mathbf{U}_\alpha) \cdot \mathbf{f}_\alpha^y(\mathbf{U}_\alpha) - \mathcal{F}_\alpha^y(\mathbf{U}_\alpha)$$

for $\alpha \in \{i, e\}$. A simple calculation results in the following expressions

$$\mathbf{V}_\alpha = \begin{pmatrix} \frac{\gamma_\alpha - s_\alpha}{\gamma_\alpha - 1} + \beta_\alpha \\ u_{x_\alpha} \Gamma_\alpha \beta_\alpha \\ u_{y_\alpha} \Gamma_\alpha \beta_\alpha \\ u_{z_\alpha} \Gamma_\alpha \beta_\alpha \\ -\Gamma_\alpha \beta_\alpha \end{pmatrix}, \quad \text{with} \quad \beta_\alpha = \frac{\rho_\alpha}{p_\alpha}, \quad (13)$$

and

$$\psi_\alpha^x = \rho_\alpha \Gamma_\alpha u_{x_\alpha}, \quad \psi_\alpha^y = \rho_\alpha \Gamma_\alpha u_{y_\alpha}. \quad (14)$$

We also introduce the following notations for jumps and averaging operations over the cell interfaces

$$\begin{aligned} \llbracket a \rrbracket_{i+\frac{1}{2},j} &= a_{i+1,j} - a_{i,j}, & \bar{a}_{i+\frac{1}{2},j} &= \frac{1}{2}(a_{i+1,j} + a_{i,j}), \\ \llbracket a \rrbracket_{i,j+\frac{1}{2}} &= a_{i,j+1} - a_{i,j}, & \bar{a}_{i,j+\frac{1}{2}} &= \frac{1}{2}(a_{i,j+1} + a_{i,j}). \end{aligned}$$

Let us first consider the homogeneous fluid part, i.e., we consider

$$\frac{\partial \mathbf{U}_\alpha}{\partial t} + \frac{\partial \mathbf{f}_\alpha^x}{\partial x} + \frac{\partial \mathbf{f}_\alpha^y}{\partial y} = 0. \quad (15)$$

109 and the corresponding semi-discrete scheme

$$\frac{d}{dt} \mathbf{U}_{\alpha,i,j}(t) + \frac{1}{\Delta x} \left(\mathbf{F}_{\alpha,i+\frac{1}{2},j}^x(t) - \mathbf{F}_{\alpha,i-\frac{1}{2},j}^x(t) \right) + \frac{1}{\Delta y} \left(\mathbf{F}_{\alpha,i,j+\frac{1}{2}}^y(t) - \mathbf{F}_{\alpha,i,j-\frac{1}{2}}^y(t) \right) = 0 \quad (16)$$

110 Then we have the following result from [39].

Theorem 4.1 (Tadmor [39]). *Let $\tilde{\mathbf{F}}_\alpha^x$ and $\tilde{\mathbf{F}}_\alpha^y$ be the consistent numerical fluxes which satisfy*

$$\llbracket \mathbf{V}_\alpha \rrbracket_{i+\frac{1}{2},j}^\top \tilde{\mathbf{F}}_{\alpha,i+\frac{1}{2},j}^x = \llbracket \psi_\alpha^x \rrbracket_{i+\frac{1}{2},j}, \quad \llbracket \mathbf{V}_\alpha \rrbracket_{i,j+\frac{1}{2}}^\top \tilde{\mathbf{F}}_{\alpha,i,j+\frac{1}{2}}^y = \llbracket \psi_\alpha^y \rrbracket_{i,j+\frac{1}{2}}, \quad (17)$$

then the scheme (16) with the numerical fluxes $\tilde{\mathbf{F}}_\alpha^x$ and $\tilde{\mathbf{F}}_\alpha^y$ is second order accurate and entropy conservative, i.e., the entropy equality

$$\frac{d}{dt} \mathcal{U}_\alpha(\mathbf{U}_{ij}) + \frac{1}{\Delta x} \left(\tilde{\mathcal{F}}_{\alpha,i+\frac{1}{2},j}^x - \tilde{\mathcal{F}}_{\alpha,i-\frac{1}{2},j}^x \right) + \frac{1}{\Delta y} \left(\tilde{\mathcal{F}}_{\alpha,i,j+\frac{1}{2}}^y - \tilde{\mathcal{F}}_{\alpha,i,j-\frac{1}{2}}^y \right) = 0,$$

is satisfied with the consistent entropy numerical fluxes,

$$\tilde{\mathcal{F}}_{\alpha,i+\frac{1}{2},j}^x = \bar{\mathbf{V}}_{\alpha,i+\frac{1}{2},j}^\top \tilde{\mathbf{F}}_{\alpha,i+\frac{1}{2},j}^x - \bar{\psi}_{\alpha,i+\frac{1}{2},j}^x, \quad \text{and} \quad \tilde{\mathcal{F}}_{\alpha,i,j+\frac{1}{2}}^y = \bar{\mathbf{V}}_{\alpha,i,j+\frac{1}{2}}^\top \tilde{\mathbf{F}}_{\alpha,i,j+\frac{1}{2}}^y - \bar{\psi}_{\alpha,i,j+\frac{1}{2}}^y.$$

111 We consider the x -directional identity of Eqn. (17) and observe that the equation (17) contains five
 112 unknowns, $\tilde{\mathbf{F}}_\alpha^x = (F_{\alpha,1}^x, F_{\alpha,2}^x, F_{\alpha,3}^x, F_{\alpha,4}^x, F_{\alpha,5}^x)^\top$. Hence, in general, we will have non-uniqueness for the
 113 solutions of this algebraic equation. Several authors [32, 40] have presented different techniques to find
 114 an affordable entropy conservative flux. We will follow the procedure of [1, 32] to derive the expression
 115 for the fluxes.

Consider the flux at $(i + \frac{1}{2}, j)$. To simplify the notation, we suppress the cell indices i, j , and let

$$\llbracket \cdot \rrbracket = (\cdot)_{i+1,j} - (\cdot)_{i,j}, \quad (\bar{\cdot}) = \frac{(\cdot)_{i,j} + (\cdot)_{i+1,j}}{2}$$

116 Define $a^{\text{ln}} = \frac{\llbracket a \rrbracket}{\llbracket \log a \rrbracket}$ as the logarithmic average for a strictly positive scalar a .

Applying the jump condition $\llbracket ab \rrbracket = \bar{a} \llbracket b \rrbracket + \bar{b} \llbracket a \rrbracket$ on the equation $\Gamma_\alpha = \frac{1}{\sqrt{1 - \mathbf{u}_\alpha^2}}$ written as $\Gamma_\alpha^2 = 1 + m_{x_\alpha}^2 + m_{y_\alpha}^2 + m_{z_\alpha}^2$, we obtain

$$\llbracket \Gamma_\alpha \rrbracket = \frac{1}{\Gamma_\alpha} (\bar{m}_{x_\alpha} \llbracket m_{x_\alpha} \rrbracket + \bar{m}_{y_\alpha} \llbracket m_{y_\alpha} \rrbracket + \bar{m}_{z_\alpha} \llbracket m_{z_\alpha} \rrbracket),$$

where, $m_{x_\alpha} = \Gamma_\alpha u_{x_\alpha}$, $m_{y_\alpha} = \Gamma_\alpha u_{y_\alpha}$ and $m_{z_\alpha} = \Gamma_\alpha u_{z_\alpha}$. Using this, we can write the jump in \mathbf{V}_α in terms of the jump in ρ_α , β_α , m_{x_α} , m_{y_α} and m_{z_α} as follows:

$$[\mathbf{V}_\alpha] = \begin{pmatrix} \frac{[\rho_\alpha]}{\rho_\alpha^{\text{in}}} + k_\alpha [\beta_\alpha] \\ \bar{m}_{x_\alpha} [\beta_\alpha] + \bar{\beta}_\alpha [m_{x_\alpha}] \\ \bar{m}_{y_\alpha} [\beta_\alpha] + \bar{\beta}_\alpha [m_{y_\alpha}] \\ \bar{m}_{z_\alpha} [\beta_\alpha] + \bar{\beta}_\alpha [m_{z_\alpha}] \\ -\bar{\Gamma}_\alpha [\beta_\alpha] - \frac{\bar{\beta}_\alpha \bar{m}_{x_\alpha}}{\bar{\Gamma}_\alpha} [m_{x_\alpha}] - \frac{\bar{\beta}_\alpha \bar{m}_{y_\alpha}}{\bar{\Gamma}_\alpha} [m_{y_\alpha}] - \frac{\bar{\beta}_\alpha \bar{m}_{z_\alpha}}{\bar{\Gamma}_\alpha} [m_{z_\alpha}] \end{pmatrix},$$

where $\beta_\alpha = \frac{\rho_\alpha}{\rho_\alpha}$, and $k_\alpha = \left(\frac{1}{\gamma - 1} \frac{1}{\beta_\alpha^{\text{in}}} + 1 \right)$. Furthermore, $[\psi_\alpha^x]$ can be written as

$$[\psi_\alpha^x] = \bar{\rho}_\alpha [m_{x_\alpha}] + \bar{m}_{x_\alpha} [\rho_\alpha].$$

and Eqn. (17) becomes

$$F_{\alpha,1}^x [V_{\alpha,1}] + F_{\alpha,2}^x [V_{\alpha,2}] + F_{\alpha,3}^x [V_{\alpha,3}] + F_{\alpha,4}^x [V_{\alpha,4}] + F_{\alpha,5}^x [V_{\alpha,5}] = [\psi_\alpha^x],$$

which simplifies to,

$$\begin{aligned} & \left(\frac{F_{\alpha,1}^x}{\rho_\alpha^{\text{in}}} \right) [\rho_\alpha] + \left(\bar{\beta}_\alpha F_{\alpha,2}^x - \frac{\bar{\beta}_\alpha \bar{m}_{x_\alpha}}{\bar{\Gamma}_\alpha} F_{\alpha,5}^x \right) [m_{x_\alpha}] + \left(\bar{\beta}_\alpha F_{\alpha,3}^x - \frac{\bar{\beta}_\alpha \bar{m}_{y_\alpha}}{\bar{\Gamma}_\alpha} F_{\alpha,5}^x \right) [m_{y_\alpha}] \\ & + \left(\bar{\beta}_\alpha F_{\alpha,4}^x - \frac{\bar{\beta}_\alpha \bar{m}_{z_\alpha}}{\bar{\Gamma}_\alpha} F_{\alpha,5}^x \right) [m_{z_\alpha}] + \left(k_\alpha F_{\alpha,1}^x + \bar{m}_{x_\alpha} F_{\alpha,2}^x + \bar{m}_{y_\alpha} F_{\alpha,3}^x + \bar{m}_{z_\alpha} F_{\alpha,4}^x - F_{\alpha,5}^x \bar{\Gamma}_\alpha \right) [\beta_\alpha] \\ & = \bar{\rho}_\alpha [m_{x_\alpha}] + \bar{m}_{x_\alpha} [\rho_\alpha]. \end{aligned}$$

We want this equation to hold for all possible values of the jumps. This is possible if the coefficients of $[\rho_\alpha]$, $[\beta_\alpha]$, $[m_{x_\alpha}]$, $[m_{y_\alpha}]$, and $[m_{z_\alpha}]$, agree on both sides, which yields the following fluxes,

$$\tilde{\mathbf{F}}_{\alpha,i+\frac{1}{2},j}^x = \tilde{\mathbf{F}}_\alpha^x(\mathbf{U}_{\alpha,i,j}, \mathbf{U}_{\alpha,i+1,j}) = \begin{pmatrix} \rho_\alpha^{\text{in}} \bar{m}_{x_\alpha} \\ \frac{1}{\bar{\beta}_\alpha} \left(\frac{\bar{\beta}_\alpha \bar{m}_{x_\alpha}}{\bar{\Gamma}_\alpha} F_{\alpha,5}^x + \bar{\rho}_\alpha \right) \\ \frac{\bar{m}_{y_\alpha}}{\bar{\Gamma}_\alpha} F_{\alpha,5}^x \\ \frac{\bar{m}_{z_\alpha}}{\bar{\Gamma}_\alpha} F_{\alpha,5}^x \\ \frac{-\bar{\Gamma}_\alpha \left(k_\alpha \rho_\alpha^{\text{in}} \bar{m}_{x_\alpha} + \frac{\bar{m}_{x_\alpha} \bar{\rho}_\alpha}{\bar{\beta}_\alpha} \right)}{(\bar{m}_{x_\alpha}^2 + \bar{m}_{y_\alpha}^2 + \bar{m}_{z_\alpha}^2 - (\bar{\Gamma}_\alpha)^2)} \end{pmatrix}_{i+\frac{1}{2},j} \quad (18)$$

It is easy to verify that $\tilde{\mathbf{F}}_\alpha^x$ is consistent with the flux \mathbf{f}_α^x . Similarly, we can derive the expression for $\tilde{\mathbf{F}}_\alpha^y$ to get

$$\tilde{\mathbf{F}}_{\alpha,i,j+\frac{1}{2}}^y = \tilde{\mathbf{F}}_\alpha^y(\mathbf{U}_{\alpha,i,j}, \mathbf{U}_{\alpha,i,j+1}) = \begin{pmatrix} \rho_\alpha^{\text{in}} \bar{m}_{y_\alpha} \\ \frac{\bar{m}_{x_\alpha}}{\bar{\Gamma}_\alpha} F_{\alpha,5}^y \\ \frac{1}{\bar{\beta}_\alpha} \left(\frac{\bar{\beta}_\alpha \bar{m}_{y_\alpha}}{\bar{\Gamma}_\alpha} F_{\alpha,5}^y + \bar{\rho}_\alpha \right) \\ \frac{\bar{m}_{z_\alpha}}{\bar{\Gamma}_\alpha} F_{\alpha,5}^y \\ \frac{-\bar{\Gamma}_\alpha \left(k_\alpha \rho_\alpha^{\text{in}} \bar{m}_{y_\alpha} + \frac{\bar{m}_{y_\alpha} \bar{\rho}_\alpha}{\bar{\beta}_\alpha} \right)}{(\bar{m}_{x_\alpha}^2 + \bar{m}_{y_\alpha}^2 + \bar{m}_{z_\alpha}^2 - (\bar{\Gamma}_\alpha)^2)} \end{pmatrix}_{i,j+\frac{1}{2}}, \quad (19)$$

117 which is consistent with \mathbf{f}_α^y .

118 **Theorem 4.2.** *The numerical scheme (10), with the numerical fluxes (18) and (19) is second-order*
 119 *accurate and entropy conservative, i.e., it satisfies (11).*

120 *Proof.* Following [39] and [30], multiplying (10) with $\mathbf{V}_{\alpha,i,j}^\top$, we get,

$$\begin{aligned} \frac{d}{dt}\mathcal{U}_\alpha(\mathbf{U}_{\alpha,i,j}) + \frac{1}{\Delta x} \left(\tilde{\mathcal{F}}_{\alpha,i+\frac{1}{2},j}^x - \tilde{\mathcal{F}}_{\alpha,i-\frac{1}{2},j}^x \right) + \frac{1}{\Delta y} \left(\tilde{\mathcal{F}}_{\alpha,i,j+\frac{1}{2}}^y - \tilde{\mathcal{F}}_{\alpha,i,j-\frac{1}{2}}^y \right) \\ = \mathbf{V}_{\alpha,i,j}^\top \cdot \mathbf{s}_\alpha(\mathbf{U}_{\alpha,i,j}(t), \mathbf{U}_{m,i,j}(t)) \end{aligned}$$

Now, we note that

$$\mathbf{V}_{\alpha,i,j}^\top \cdot \mathbf{s}_\alpha(\mathbf{U}_{\alpha,i,j}(t), \mathbf{U}_{m,i,j}(t)) = 0$$

121 to arrive at the equality (11). \square

The entropy conservative fluxes derived above are only second-order accurate. Following [41], we can use second-order fluxes to construct $2p^{\text{th}}$ -order accurate fluxes for any positive integer p . In particular, the 4th-order ($p = 2$) x -directional entropy conservative flux $\tilde{\mathbf{F}}_{\alpha,i+\frac{1}{2},j}^{x,4}$ is given by,

$$\tilde{\mathbf{F}}_{\alpha,i+\frac{1}{2},j}^{x,4} = \frac{4}{3}\tilde{\mathbf{F}}_\alpha^x(\mathbf{U}_{\alpha,i,j}, \mathbf{U}_{\alpha,i+1,j}) - \frac{1}{6}\left(\tilde{\mathbf{F}}_\alpha^x(\mathbf{U}_{\alpha,i-1,j}, \mathbf{U}_{\alpha,i+1,j}) + \tilde{\mathbf{F}}_\alpha^x(\mathbf{U}_{\alpha,i,j}, \mathbf{U}_{\alpha,i+2,j})\right).$$

122 Similarly, we can obtain the fourth-order entropy conservative flux $\tilde{\mathbf{F}}_{\alpha,i+\frac{1}{2},j}^{y,4}$ in y -direction. Combining
123 this we have the following remarks.

124 **Remark 4.1.** Replacing second-order fluxes with the higher-order fluxes in (10), we arrive at high-order,
125 entropy conservative schemes.

126 **Remark 4.2.** The result from [41] gives only even order accurate fluxes. So, for q^{th} -order (q is an odd
127 integer) accurate scheme, we use a $(q + 1)^{\text{th}}$ -order (an even number) accurate flux.

128 4.1.2 High-order entropy stable schemes for fluid equations

The entropy conservative schemes presented above will produce high-frequency oscillations near the shocks as they are central fluxes which do not dissipate entropy. Following [39], we introduce modified fluxes which will ensure entropy dissipation at the shocks. We consider a modified numerical flux of the form,

$$\begin{aligned} \mathbf{F}_{\alpha,i+\frac{1}{2},j}^x &= \tilde{\mathbf{F}}_{\alpha,i+\frac{1}{2},j}^x - \frac{1}{2}\mathbf{D}_{\alpha,i+\frac{1}{2},j}^x \llbracket \mathbf{V}_\alpha \rrbracket_{i+\frac{1}{2},j}, \\ \mathbf{F}_{\alpha,i,j+\frac{1}{2}}^y &= \tilde{\mathbf{F}}_{\alpha,i,j+\frac{1}{2}}^y - \frac{1}{2}\mathbf{D}_{\alpha,i,j+\frac{1}{2}}^y \llbracket \mathbf{V}_\alpha \rrbracket_{i,j+\frac{1}{2}}, \end{aligned} \quad (20)$$

129 where $\mathbf{D}_{\alpha,i+\frac{1}{2},j}^x$ and $\mathbf{D}_{\alpha,i,j+\frac{1}{2}}^y$ are symmetric positive definite matrices. Then we have the following
130 Lemma:

Lemma 4.1 (Tadmor [39]). *The numerical scheme (8) with the numerical fluxes (20) is entropy stable, i.e., the entropy inequality*

$$\frac{d}{dt}\mathcal{U}_\alpha(\mathbf{U}_{ij}) + \frac{1}{\Delta x} \left(\hat{\mathcal{F}}_{\alpha,i+\frac{1}{2},j}^x - \hat{\mathcal{F}}_{\alpha,i-\frac{1}{2},j}^x \right) + \frac{1}{\Delta y} \left(\hat{\mathcal{F}}_{\alpha,i,j+\frac{1}{2}}^y - \hat{\mathcal{F}}_{\alpha,i,j-\frac{1}{2}}^y \right) \leq 0, \quad \alpha \in \{i, e\},$$

is satisfied with the consistent numerical entropy flux functions,

$$\begin{aligned} \hat{\mathcal{F}}_{\alpha,i+\frac{1}{2},j}^x &= \tilde{\mathcal{F}}_{\alpha,i+\frac{1}{2},j}^x + \frac{1}{2}(\bar{\mathbf{V}}_\alpha)_{i+\frac{1}{2},j}^\top \mathbf{D}_{\alpha,i+\frac{1}{2},j}^x \llbracket \mathbf{V}_\alpha \rrbracket_{i+\frac{1}{2},j}, \\ \hat{\mathcal{F}}_{\alpha,i,j+\frac{1}{2}}^y &= \tilde{\mathcal{F}}_{\alpha,i,j+\frac{1}{2}}^y + \frac{1}{2}(\bar{\mathbf{V}}_\alpha)_{i,j+\frac{1}{2}}^\top \mathbf{D}_{\alpha,i,j+\frac{1}{2}}^y \llbracket \mathbf{V}_\alpha \rrbracket_{i,j+\frac{1}{2}}. \end{aligned}$$

We will use *Rusanov type* diffusion operators for the matrix \mathbf{D}_α , which is given by,

$$\mathbf{D}_{\alpha,i+\frac{1}{2},j}^x = \tilde{\mathbf{R}}_{\alpha,i+\frac{1}{2},j}^x \Lambda_{\alpha,i+\frac{1}{2},j}^x \tilde{\mathbf{R}}_{\alpha,i+\frac{1}{2},j}^{x\top}, \quad \text{and} \quad \mathbf{D}_{\alpha,i,j+\frac{1}{2}}^y = \tilde{\mathbf{R}}_{\alpha,i,j+\frac{1}{2}}^y \Lambda_{\alpha,i,j+\frac{1}{2}}^y \tilde{\mathbf{R}}_{\alpha,i,j+\frac{1}{2}}^{y\top}. \quad (21)$$

where $\tilde{\mathbf{R}}_\alpha^d$, $d \in \{x, y\}$, are matrices of the entropy scaled right eigenvectors and Λ_α^d are 5×5 diagonal matrices of the form

$$\Lambda_\alpha^d = \left(\max_{1 \leq k \leq 5} |\Lambda_{\alpha_k}^d| \right) \mathbf{I}_{5 \times 5},$$

where $\{\Lambda_{\alpha_k}^d : 1 \leq k \leq 5\}$, $d \in \{x, y\}$, are the eigenvalues of the flux Jacobian. Following [42], we have $\partial_{\mathbf{V}_\alpha} \mathbf{U}_\alpha = \tilde{\mathbf{R}}_\alpha^d (\tilde{\mathbf{R}}_\alpha^d)^\top$ for $d \in \{x, y\}$, hence,

$$\tilde{\mathbf{R}}_\alpha^d \Lambda_\alpha^d (\tilde{\mathbf{R}}_\alpha^d)^{(-1)} [\mathbf{U}_\alpha] \approx \tilde{\mathbf{R}}_\alpha^d \Lambda_\alpha^d (\tilde{\mathbf{R}}_\alpha^d)^{(-1)} \partial_{\mathbf{V}_\alpha} \mathbf{U}_\alpha [\mathbf{V}_\alpha] = \tilde{\mathbf{R}}_\alpha^d \Lambda_\alpha^d (\tilde{\mathbf{R}}_\alpha^d)^\top [\mathbf{V}_\alpha],$$

131 i.e., the entropy diffusion operator used here is similar to the *Roe* diffusion operator when the entropy
132 scaled right eigenvectors are used. The complete expressions for $\tilde{\mathbf{R}}_\alpha^d$ are derived in Appendix (B.2).

With the choice of diffusion operator (21), the numerical scheme (8) with the numerical flux (20) is entropy stable. However, the scheme is only first-order accurate due to the presence of the first-order jump terms $[\mathbf{V}_\alpha]_{i+\frac{1}{2},j}$ and $[\mathbf{V}_\alpha]_{i,j+\frac{1}{2}}$. A straightforward way to increase the order of accuracy is to approximate the jumps in the diffusive term of (20) using a higher-order reconstruction process. However, proving the entropy stability of the resulting scheme is not possible. Instead, we follow the process prescribed in [30] and introduce the *scaled entropy variables*. We illustrate the procedure for the x -direction only, as the y -directional case is similar. Define the change of variables

$$\mathcal{V}_{\alpha,m,j}^{x,\pm} = (\tilde{\mathbf{R}}_{\alpha,i\pm\frac{1}{2},j}^x)^\top \mathbf{V}_{\alpha,m,j}, \quad m \text{ are neighbours of cell } (i,j) \text{ along } x$$

Using ENO procedure we choose a stencil of cells and construct the polynomials $P_{i,j}^{x,\pm}(x)$ of degree k and evaluate it at the faces of cell (i,j)

$$\tilde{\mathcal{V}}_{\alpha,i,j}^{x,\pm} = P_{i,j}^{x,\pm}(x_{i\pm\frac{1}{2}})$$

Converting back to the entropy variables,

$$\tilde{\mathbf{V}}_{\alpha,i,j}^{x,\pm} = \left\{ (\tilde{\mathbf{R}}_{\alpha,i\pm\frac{1}{2},j}^x)^\top \right\}^{(-1)} \tilde{\mathcal{V}}_{\alpha,i,j}^{x,\pm}$$

are the corresponding k -th order reconstructed values for \mathbf{V}_α . Hence the high-order entropy stable numerical flux is given by,

$$\mathbf{F}_{\alpha,i+\frac{1}{2},j}^{x,k} = \tilde{\mathbf{F}}_{\alpha,i+\frac{1}{2},j}^{x,2p} - \frac{1}{2} \mathbf{D}_{\alpha,i+\frac{1}{2},j}^x [\tilde{\mathbf{V}}_\alpha]_{i+\frac{1}{2},j} \quad (22)$$

where $[\tilde{\mathbf{V}}_\alpha]_{i+\frac{1}{2},j}$ stands for,

$$[\tilde{\mathbf{V}}_\alpha]_{i+\frac{1}{2},j} = \tilde{\mathbf{V}}_{\alpha,i+1,j}^{x,-} - \tilde{\mathbf{V}}_{\alpha,i,j}^{x,+}.$$

133 As only even order entropy conservative fluxes $\tilde{\mathbf{F}}_{\alpha,i+\frac{1}{2},j}^{x,2p}$ are available, we choose $p \in \mathbb{N}$ as

- 134 • $p = k/2$ if k is even,
- 135 • $p = (k+1)/2$ if k is odd,

136 where k is the order of the scheme. Following [30], a sufficient condition for the numerical flux (22)
137 to be entropy stable is that the reconstruction process for \mathcal{V} must satisfy the *sign preserving property*.
138 For the second-order reconstruction, we use the *min-mod* reconstruction, which satisfies this property.
139 Following [31], we use ENO reconstruction as it satisfies the *sign preserving property*. For third and
140 fourth-order schemes, we use fourth-order entropy conservative flux along with the third and fourth-
141 order ENO reconstruction of the scaled entropy variables. We now have the following result:

142 **Theorem 4.3.** *The numerical scheme (10) with entropy stable flux (22) and ENO reconstruction satisfies*
143 *the entropy inequality (12).*

Proof. The proof follows from [30] using the fact that,

$$\mathbf{V}_{\alpha,i,j}^\top \cdot \mathbf{s}_\alpha(\mathbf{U}_{\alpha,i,j}(t), \mathbf{U}_{\alpha,m,i,j}(t)) = 0$$

144 and the sign property of ENO reconstruction. □

145 **Remark 4.3.** *The above result holds for any discretization of Maxwell's equations.*

146 4.2 Discretization of Maxwell's equations

To spatially discretize the Maxwell's equations (1g)-(1j), we use the finite-difference scheme based on the Rusanov solver. The x - and y -directional numerical fluxes are given by

$$\begin{aligned}\mathbf{F}_{m,i+\frac{1}{2},j}^x &= \frac{1}{2}(\mathbf{f}_m^x(\mathbf{U}_{m,i,j}) + \mathbf{f}_m^x(\mathbf{U}_{m,i+1,j})) - \frac{c}{2}(\mathbf{U}_{m,i+1,j} - \mathbf{U}_{m,i,j}), \\ \mathbf{F}_{m,i,j+\frac{1}{2}}^y &= \frac{1}{2}(\mathbf{f}_m^y(\mathbf{U}_{m,i,j}) + \mathbf{f}_m^y(\mathbf{U}_{m,i,j+1})) - \frac{c}{2}(\mathbf{U}_{m,i,j+1} - \mathbf{U}_{m,i,j}).\end{aligned}$$

147 where $c = 1$ is the speed of light. To obtain higher accuracy, we use *min-mod* limiter [25] to reconstruct
148 the variables \mathbf{U}_m at the cell faces to get the second-order scheme. Furthermore, we use third and
149 fifth-order WENO reconstructions [43] to obtain the third- and fourth-order Rusanov's solver for the
150 Maxwell's equations.

151 5 Fully discrete scheme

Let \mathbf{U}^n be the discrete solution at time t^n , where the time step is $\Delta t = t^{n+1} - t^n$. The semi-discrete scheme (8) can be expressed as

$$\frac{d}{dt}\mathbf{U}_{i,j}(t) = \mathcal{L}_{i,j}(\mathbf{U}(t)) + \mathbf{s}(\mathbf{U}_{i,j}(t)), \quad \mathbf{U}_{i,j}(t^n) = \mathbf{U}_{i,j}^n \quad (24)$$

where,

$$\mathcal{L}_{i,j}(\mathbf{U}(t)) = -\frac{1}{\Delta x} \left(\mathbf{F}_{i+\frac{1}{2},j}^x(t) - \mathbf{F}_{i-\frac{1}{2},j}^x(t) \right) - \frac{1}{\Delta y} \left(\mathbf{F}_{i,j+\frac{1}{2}}^y(t) - \mathbf{F}_{i,j-\frac{1}{2}}^y(t) \right).$$

152 We propose fully explicit and IMEX schemes for the above system.

153 5.1 Explicit schemes

154 For the explicit time discretizations, we use explicit strong stability preserving Runge Kutta (SSP-RK)
155 methods [44]. The second and third-order accurate SSP-RK schemes are given as follows.

- 156 1. Set $\mathbf{U}^0 = \mathbf{U}^n$.
2. For $m = 1, \dots, k + 1$, compute,

$$\mathbf{U}_{i,j}^{(m)} = \sum_{l=0}^{m-1} \left[\alpha_{ml} \mathbf{U}_{i,j}^{(l)} + \beta_{ml} \Delta t (\mathcal{L}_{i,j}(\mathbf{U}^{(l)}) + \mathbf{s}(\mathbf{U}_{i,j}^{(l)})) \right]$$

157 where α_{ml} and β_{ml} are given in Table (1).

- 158 3. Finally, $\mathbf{U}_{i,j}^{n+1} = \mathbf{U}_{i,j}^{(k+1)}$.

Order	α_{il}		β_{il}		
2	1		1		
	1/2	1/2	0	1/2	
3	1		1		
	3/4	1/4	0	1/4	
	1/3	0	2/3	0	2/3

Table 1: Coefficients for SSP Runge-Kutta time stepping

The fourth order RK-SSP is given by,

$$\begin{aligned}
\mathbf{U}_{i,j}^{(1)} &= \mathbf{U}_{i,j}^n + 0.39175222700392 (\Delta t) (\mathcal{L}_{i,j}(\mathbf{U}^n) + \mathbf{s}(\mathbf{U}_{i,j}^n)), \\
\mathbf{U}_{i,j}^{(2)} &= 0.44437049406734 \mathbf{U}_{i,j}^n + 0.55562950593266 \mathbf{U}_{i,j}^{(1)} \\
&\quad + 0.36841059262959 (\Delta t) (\mathcal{L}_{i,j}(\mathbf{U}^{(1)}) + \mathbf{s}(\mathbf{U}_{i,j}^{(1)})), \\
\mathbf{U}_{i,j}^{(3)} &= 0.62010185138540 \mathbf{U}_{i,j}^n + 0.37989814861460 \mathbf{U}_{i,j}^{(2)} \\
&\quad + 0.25189177424738 (\Delta t) (\mathcal{L}_{i,j}(\mathbf{U}^{(2)}) + \mathbf{s}(\mathbf{U}_{i,j}^{(2)})), \\
\mathbf{U}_{i,j}^{(4)} &= 0.17807995410773 \mathbf{U}_{i,j}^n + 0.82192004589227 \mathbf{U}_{i,j}^{(3)} \\
&\quad + 0.54497475021237 (\Delta t) (\mathcal{L}_{i,j}(\mathbf{U}^{(3)}) + \mathbf{s}(\mathbf{U}_{i,j}^{(3)})), \\
\mathbf{U}_{i,j}^{n+1} &= 0.00683325884039 \mathbf{U}^n + 0.51723167208978 \mathbf{U}_{i,j}^{(2)} + 0.12759831133288 \mathbf{U}_{i,j}^{(3)} \\
&\quad + 0.34833675773694 \mathbf{U}_{i,j}^{(4)} + 0.08460416338212 (\Delta t) (\mathcal{L}_{i,j}(\mathbf{U}^{(3)}) + \mathbf{s}(\mathbf{U}_{i,j}^{(3)})) \\
&\quad + 0.22600748319395 (\Delta t) (\mathcal{L}_{i,j}(\mathbf{U}^{(4)}) + \mathbf{s}(\mathbf{U}_{i,j}^{(4)})).
\end{aligned}$$

159 We use a second-order spatial accurate scheme with a second-order explicit time scheme, which is denoted
160 by, **O2-ES-Exp**. Similarly, the third-order spatial accurate scheme is time-discretized with the third-
161 order RK method above and denoted by, **O3-ES-Exp**. The fourth-order scheme consists of fourth-order
162 spatial discretization with the fourth-order time update above and denoted by **O4-ES-Exp**.

163 5.2 ARK-IMEX schemes

The source terms are stiff when the charge to mass ratio r_α is large, which results in a time-step restriction when using explicit time integration schemes. To overcome this difficulty, we will use the Additive Runge Kutta Implicit Explicit (ARK IMEX) time stepping scheme from [45]. Here, the flux terms will be treated explicitly, and the source terms will be treated implicitly. We write the semi-discrete scheme (8) in a simplified form as follows

$$\frac{\partial \mathbf{U}}{\partial t} = F_{NS}(\mathbf{U}(t)) + F_S(\mathbf{U}(t)),$$

164 where $F_{NS}(\mathbf{U}(t)) = \mathcal{L}_{i,j}(\mathbf{U}(t))$ denotes the non-stiff flux terms, and $F_S(\mathbf{U}(t)) = \mathbf{s}(\mathbf{U}_{i,j}(t))$ denotes the
165 stiff source terms. Note that the source terms contain only the solution value in the parent cell and not
166 any spatial derivatives, and hence they do not depend on the solution in neighboring cells.

167 5.2.1 Second order time discretization.

For the second-order discretization, we use L-Stable second-order accurate ARK IMEX scheme from [45]. The method has two implicit stages and is given by

$$\begin{aligned}
\mathbf{U}^{(1)} &= \mathbf{U}^n + \Delta t (\beta F_S(\mathbf{U}^{(1)}(t^n))), \\
\mathbf{U}^{(2)} &= \mathbf{U}^n + \Delta t (F_{NS}(\mathbf{U}^{(1)}(t^n)) + (1 - 2\beta)F_S(\mathbf{U}^{(1)}(t^n)) + \beta F_S(\mathbf{U}^{(2)}(t^n))), \\
\mathbf{U}^{(n+1)} &= \mathbf{U}^n + \Delta t \left(\frac{1}{2}F_{NS}(\mathbf{U}^{(1)}(t^n)) + \frac{1}{2}F_{NS}(\mathbf{U}^{(2)}(t^n)) + \frac{1}{2}F_S(\mathbf{U}^{(1)}(t^n)) + \frac{1}{2}F_S(\mathbf{U}^{(2)}(t^n)) \right),
\end{aligned}$$

168 where $\beta = 1 - \frac{1}{\sqrt{2}}$. Note that, to evaluate $\mathbf{U}^{(1)}$ and $\mathbf{U}^{(2)}$, we need to solve a nonlinear system of algebraic
169 equations. However, the resulting equations are only local, i.e., we get an independent set of equations
170 for each cell. We solve these equations using the Newton's method, where the convergence and the next
171 direction search is based on the backtracing line search framework. A detailed procedure is given in [46].
172 In the higher-order method, we will use the same process to update the internal IMEX steps.

173 5.2.2 Third and fourth-order time discretization.

174 For the higher-order discretization, we use L-Stable ARK IMEX methods from [47]. We ignore the
175 subscripts $\{i, j\}$ for simplicity. The ARK scheme from [47] has the following steps.

- 176 1. Set $\mathbf{U}^0 = \mathbf{U}^n$.
2. For $m = 1, \dots, k$, compute,

$$\mathbf{U}^{(m)} = \mathbf{U}^n + \Delta t \sum_{l=0}^{m-1} a_{ml}^{[NS]} F_{NS}(\mathbf{U}^l) + \Delta t \sum_{l=0}^m a_{ml}^{[S]} F_S(\mathbf{U}^l),$$

177 where, $\mathbf{U}^{(m)}$ approximates $\mathbf{U}(t^n + c_m \Delta t)$.

3. Finally,

$$\mathbf{U}^{n+1} = \mathbf{U}^n + \Delta t \sum_{l=0}^k b_l^{[NS]} F_{NS}(\mathbf{U}^l) + \Delta t \sum_{l=0}^k b_l^{[S]} F_S(\mathbf{U}^l),$$

178 where k is the order of the desired time discretization (k ranges from 3 to 5), and coefficients $a_{ml}^{[NS]}$,
179 $a_{ml}^{[S]}$, $b_l^{[NS]}$, $b_l^{[S]}$, c_l are defined accordingly by the order of accuracy and stability considerations.

180 We present coefficients for the third-order scheme in Appendix (C). The coefficients for the fourth-order
181 time update can be found in [47]. We denote the second-order IMEX scheme with **O2-ES-IMEX**,
182 third-order IMEX scheme with **O3-ES-IMEX** and fourth-order IMEX scheme with **O4-ES-IMEX**.

183 6 Numerical results

184 In this section, we present numerical results for various test cases. We set specific heat ratios $\gamma_i = \gamma_e =$
185 $4/3$, unless stated otherwise. In all the test cases, we take initial values of the potentials ϕ and ψ to
186 be zero and potential speeds $\kappa = \chi = 1$. In some test cases, we need to consider the resistive effects;
187 following [12], we modify the momentum (1b), (1e) and energy equations (1c), (1f) for the fluid parts by
188 adding resistive terms as follows,

$$\frac{\partial(\rho_\alpha h_\alpha \Gamma_\alpha^2 \mathbf{u}_\alpha)}{\partial t} + \nabla \cdot (\rho_\alpha h_\alpha \Gamma_\alpha^2 \mathbf{u}_\alpha \mathbf{u}_\alpha^\top + p_\alpha \mathbf{I}) = r_\alpha \Gamma_\alpha \rho_\alpha (\mathbf{E} + \mathbf{u}_\alpha \times \mathbf{B}) + \mathbf{R}_\alpha, \quad (27a)$$

$$\frac{\partial(\mathcal{E}_\alpha)}{\partial t} + \nabla \cdot ((\mathcal{E}_\alpha + p_\alpha) \mathbf{u}_\alpha) = r_\alpha \Gamma_\alpha \rho_\alpha (\mathbf{u}_\alpha \cdot \mathbf{E}) + R_\alpha^0, \quad (27b)$$

for $\alpha \in \{i, e\}$. Following [12], an anti-symmetry relationship, $(\mathbf{R}_e, R_e^0) = (-\mathbf{R}_i, -R_i^0)$, has been assumed
for the conservation of the total momentum and energy density. The expressions for the terms \mathbf{R}_i and
 R_i^0 are given by

$$\mathbf{R}_i = -\eta \frac{\omega_p^2}{r_i - r_e} (\mathbf{j} - \rho_0 \Phi), \quad R_i^0 = -\eta \frac{\omega_p^2}{r_i - r_e} (\rho_c - \rho_0 \Lambda),$$

189 where,

$$\begin{aligned} \omega_p^2 &= r_i^2 \rho_i + r_e^2 \rho_e, & \Phi &= \frac{r_i \rho_i \Gamma_i \mathbf{u}_i + r_e \rho_e \Gamma_e \mathbf{u}_e}{\omega_p^2}, \\ \Lambda &= \frac{r_i^2 \rho_i \Gamma_i + r_e^2 \rho_e \Gamma_e}{\omega_p^2}, & \rho_0 &= \Lambda \rho_c - \mathbf{j} \cdot \Phi \end{aligned} \quad (28)$$

190 Here η is the resistivity constant and ω_p is the total plasma frequency. The total plasma skin depth d_p
191 is defined as $d_p = \frac{1}{\omega_p}$. For the time update using ARK IMEX scheme, we couple the resistive terms with
192 the other source terms and treat them implicitly, i.e., we modify F_S to include the resistive terms.

To compare the numerical results with published work consistently, for all the test cases taken from [29], we multiply the source term for Maxwell's equations by 4π , i.e., we consider,

$$\mathbf{s}_m = 4\pi \begin{pmatrix} 0 \\ 0 \\ 0 \\ -j_x \\ -j_y \\ -j_z \\ \chi\rho_c \\ 0 \end{pmatrix}. \quad (29)$$

193 Consequently, in the test cases from [29], the total plasma skin depth is given by $d_p = \frac{\sqrt{2}}{\omega_p}$ with $\omega_p^2 =$
 194 $4\pi(r_i^2\rho_i + r_e^2\rho_e)$.

195 6.1 One-dimensional test cases

For the one-dimensional test cases, the time step is chosen using

$$\Delta t = \text{CFL} \cdot \min \left\{ \frac{\Delta x}{\Lambda_{max}^x(\mathbf{U}_i)} : 1 \leq i \leq N_x \right\}, \text{ where } \Lambda_{max}^x(\mathbf{U}_i) = \max\{|\Lambda_k^x(\mathbf{U}_i)| : 1 \leq k \leq 18\}.$$

196 We take CFL to be 0.8, for the explicit (**O2-ES-Exp**, **O3-ES-Exp** and **O4-ES-Exp**), and ARK IMEX
 197 schemes (**O2-ES-IMEX**, **O3-ES-IMEX** and **O4-ES-IMEX**), unless stated otherwise.

198 6.1.1 Accuracy test

Number of cells	O2-ES-Exp		O3-ES-Exp		O4-ES-Exp	
	L^1 error	Order	L^1 error	Order	L^1 error	Order
50	4.65050e-02	–	1.45793e-03	–	1.49240e-04	–
100	1.46231e-02	1.6691	2.11487e-04	2.7853	1.13502e-05	3.7168
200	4.06705e-03	1.8462	2.68696e-05	2.9765	8.01398e-07	3.8241
400	1.10159e-03	1.8844	3.38714e-06	2.9878	5.55355e-08	3.8510
800	2.96489e-04	1.8935	4.12164e-07	3.0388	3.74592e-09	3.8900
1600	7.83571e-05	1.9198	4.74082e-08	3.1200	2.48382e-10	3.9147
3200	2.04466e-05	1.9382	5.12307e-09	3.2101	1.77044e-11	3.8104

Table 2: **Accuracy test**: L^1 errors and order of convergence for ρ_i using the explicit entropy stable schemes **O2-ES-Exp**, **O3-ES-Exp** and **O4-ES-Exp**.

To test the accuracy and order of convergence of the proposed scheme, we consider a test case with smooth solution. We follow a forced solution approach of [15] to modify the smooth test case from [1]. We add forcing term $\mathcal{S}(x, t)$ to write the one-dimensional modified system (3) as

$$\frac{\partial \mathbf{U}}{\partial t} + \frac{\partial \mathbf{f}^x}{\partial x} = \mathbf{s} + \mathcal{S}(x, t)$$

with

$$\mathcal{S}(x, t) = \left(\mathbf{0}_{13}, -\frac{1}{\sqrt{3}}(2 + \sin(2\pi(x - 0.5t))), 0, -3\pi \cos(2\pi(x - 0.5t)), \frac{2}{\sqrt{3}}(2 + \sin(2\pi(x - 0.5t))), 0 \right)^\top.$$

199 The initial ion and electron densities are $\rho_i = \rho_e = 2 + \sin(2\pi x)$, with initial velocities $u_{x_i} = u_{x_e} = 0.5$
 200 and initial pressures $p_i = p_e = 1$. The y -magnetic component is $B_y = 2 \sin(2\pi(x))$ and the z -electric
 201 field component is $E_z = -\sin(2\pi(x))$. All other primitive variables are set to zero. The computational

Number of cells	O2-ES-IMEX		O3-ES-IMEX		O4-ES-IMEX	
	L^1 error	Order	L^1 error	Order	L^1 error	Order
–						
50	4.65793e-02	–	1.47651e-03	–	1.49978e-04	–
100	1.45983e-02	1.6739	2.12698e-04	2.7953	1.13298e-05	3.7266
200	4.05330e-03	1.8486	2.70403e-05	2.9756	7.99773e-07	3.8244
400	1.09574e-03	1.8872	3.40147e-06	2.9909	5.54390e-08	3.8506
800	2.94528e-04	1.8954	4.13433e-07	3.0404	3.73935e-09	3.8900
1600	7.77465e-05	1.9216	4.75597e-08	3.1198	2.47509e-10	3.9172
3200	2.02807e-05	1.9387	5.14011e-09	3.2099	1.63939e-11	3.9162

Table 3: **Accuracy test**: L^1 errors and order of convergence for ρ_i using the ARK IMEX entropy stable schemes **O2-ES-IMEX**, **O3-ES-IMEX** and **O4-ES-IMEX**.

202 domain is $I = [0, 1]$ with periodic boundary conditions. The charge to mass ratios are $r_i = 1$ and
203 $r_e = -2$, consequently we have non-zero electric field source term \mathbf{j} . The ion-electron adiabatic index is
204 $\gamma = 5/3$. For this problem, it is easy to verify that the exact solution is $\rho_i = \rho_e = 2 + \sin(2\pi(x - 0.5t))$.

205 In Table (2) and Table (3), we have presented the L^1 -errors for ρ_i at different resolutions for ex-
206 plicit (**O2-ES-Exp**, **O3-ES-Exp** and **O4-ES-Exp**) and ARK-IMEX schemes (**O2-ES-IMEX**, **O3-
207 ES-IMEX**, and **O4-ES-IMEX**) at the final time $t = 2.0$. For both explicit and IMEX schemes, we
208 observe a consistent order of accuracy at various resolutions. Furthermore, we also note that the errors
209 for both explicit and IMEX schemes of same order are comparable at a given resolution.

210 6.1.2 Relativistic Brio–Wu test problem with finite plasma skin depth

This is a shock tube problem with finite plasma skin depth from [12, 29] and is a two-fluid extension of
the relativistic analogue of the Brio-Wu shock tube problem given in [7]. Maxwell’s source terms (29) are
included, but no resistive effects are considered. The computational domain is $[-0.5, 0.5]$ with Neumann
boundary conditions at both boundaries. The initial discontinuity is assumed to be placed at $x = 0.0$.
Following [29], the initial Riemann data is given by,

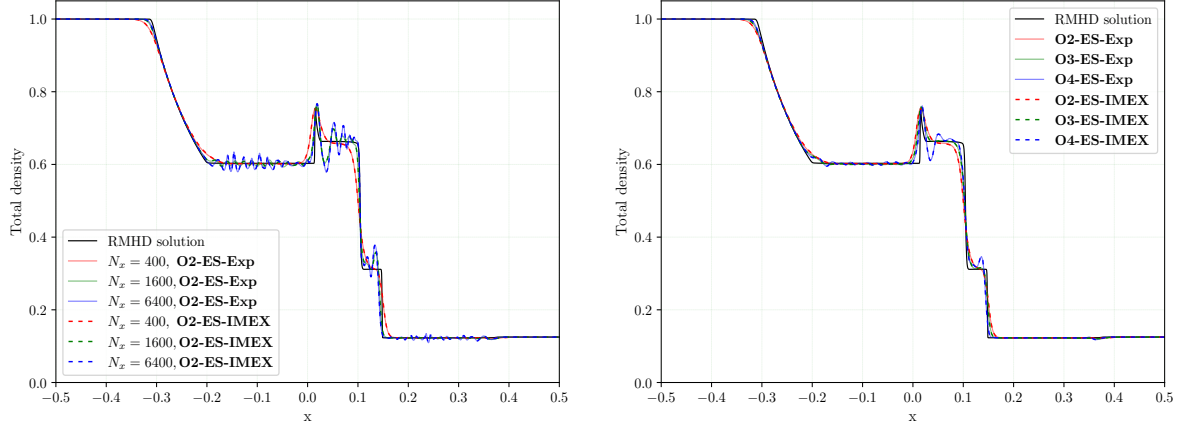
$$\mathbf{W}_L = \begin{pmatrix} \rho_i \\ p_i \\ \rho_e \\ p_e \\ B_x \\ B_y \end{pmatrix}_L = \begin{pmatrix} 0.5 \\ 0.5 \\ 0.5 \\ 0.5 \\ \sqrt{\pi} \\ \sqrt{4\pi} \end{pmatrix}, \quad \mathbf{W}_R = \begin{pmatrix} \rho_i \\ p_i \\ \rho_e \\ p_e \\ B_x \\ B_y \end{pmatrix}_R = \begin{pmatrix} 0.0625 \\ 0.05 \\ 0.0625 \\ 0.05 \\ \sqrt{\pi} \\ -\sqrt{4\pi} \end{pmatrix}.$$

211 All other variables are set to zero. Following [29], the specific heat ratios are set to $\gamma_i = \gamma_e = 2.0$, and
212 we compute the solution till final time $t = 0.4$.

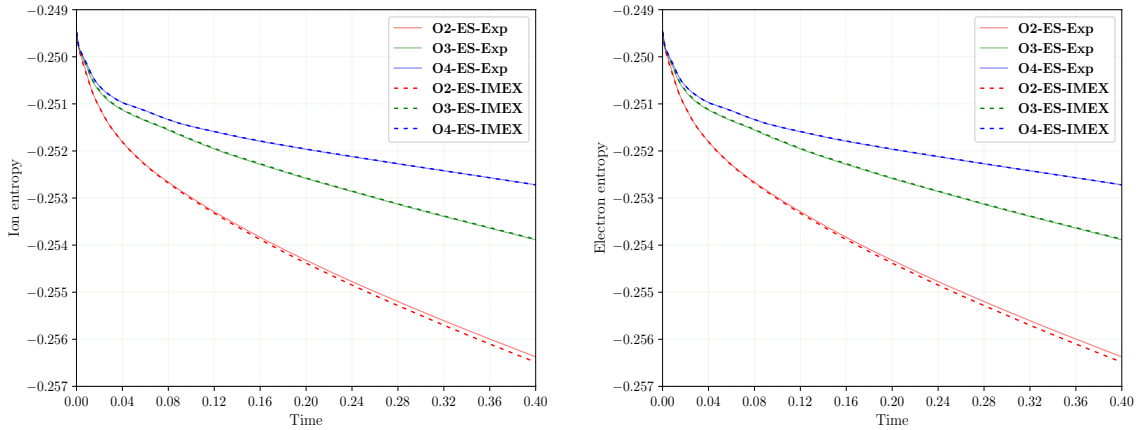
213 First, we consider charge to mass ratios as $r_i = -r_e = 10^3/\sqrt{4\pi}$, thus the plasma skin depth is
214 $10^{-3}/\sqrt{\rho_i}$. Consequently, we expect solutions to be close to the RMHD results whenever the resolution
215 of the cells is larger than the plasma skin depth.

216 To compare with the results of [29], in Figure (1(a)), we plot the total density $\rho_i + \rho_e$ for **O2-
217 ES-Exp** and **O2-ES-IMEX** schemes using 400, 1600 and 6400 cells. To compare the solution with
218 RMHD solution, we have computed “RMHD” solution using $r_i = -r_e = 10^5/\sqrt{4\pi}$ at 6400 cells and
219 **O2-ES-IMEX** scheme. We observe that on a resolution of 400 cells, the cell size $\Delta x = 0.0025$ is slightly
220 larger than the plasma skin depth in the entire domain; thus, the profile roughly matches with the
221 RMHD results [7], while at the higher resolutions, 1600 and 6400, the cell size is much smaller than
222 the plasma skin depth, consequently, appearance of the two-fluid effect in the form of dispersive waves
223 is observed. We also note that both explicit (**O2-ES-Exp**) and IMEX (**O2-ES-IMEX**) schemes have
224 similar performance in capturing all the waves and additional effects at the various resolutions.

225 To compare second-order schemes, with the third and fourth-order schemes, in Figure (1(b)), we
226 plot total density for explicit (**O2-ES-Exp**, **O3-ES-Exp** and **O4-ES-Exp**) and ARK-IMEX schemes
227 (**O2-ES-IMEX**, **O3-ES-IMEX**, and **O4-ES-IMEX**) using 400 cells. We observe that the third and

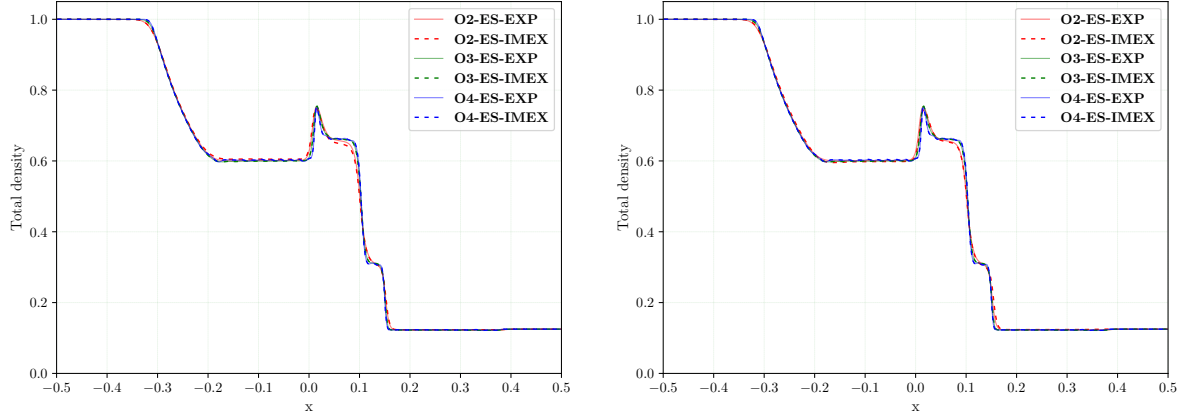


(a) Plots of total density $\rho_i + \rho_e$ for second-order schemes (**O2-ES-Exp** and **O2-ES-IMEX**) using 400, 1600 and 6400 cells. (b) Plots of total density $\rho_i + \rho_e$, for second (**O2-ES-Exp** and **O2-ES-IMEX**), third (**O3-ES-Exp** and **O3-ES-IMEX**), and fourth (**O4-ES-Exp** and **O4-ES-IMEX**) order schemes using 400 cells.

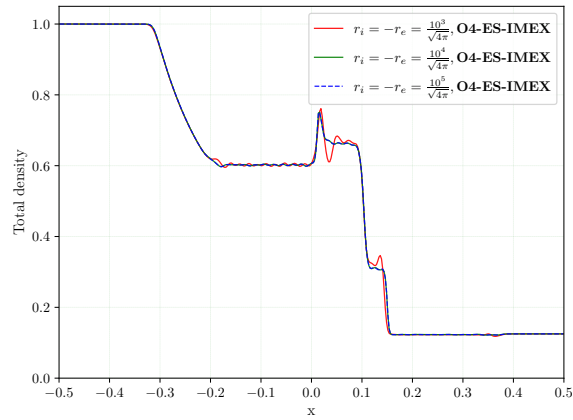


(c) Plots of total ion entropy for second (**O2-ES-Exp** and **O2-ES-IMEX**), third (**O3-ES-Exp** and **O3-ES-IMEX**), and fourth (**O4-ES-Exp** and **O4-ES-IMEX**) order schemes using 400 cells. (d) Plots of total electron entropy for second (**O2-ES-Exp** and **O2-ES-IMEX**), third (**O3-ES-Exp** and **O3-ES-IMEX**), and fourth (**O4-ES-Exp** and **O4-ES-IMEX**) order schemes using 400 cells.

Figure 1: Numerical results for **Relativistic Brio–Wu test problem with finite plasma skin depth** using different schemes and grid resolutions.



(a) Plots of total density $\rho_i + \rho_e$, for second (**O2-ES-Exp** and **O2-ES-IMEX**), third (**O3-ES-Exp** and **O3-ES-IMEX**), and fourth (**O4-ES-Exp** and **O4-ES-IMEX**) order schemes with $r_i = -r_e = 10^4 / \sqrt{4\pi}$ using **IMEX** order schemes with $r_i = -r_e = 10^5 / \sqrt{4\pi}$ using 400 cells.



(c) Plots of total density $\rho_i + \rho_e$, for **O4-ES-IMEX** scheme for various stiff cases at 400 cells.

Figure 2: Numerical results for Relativistic Brio–Wu test problem with finite plasma skin depth using various stiff cases at 400 cells.

228 fourth-order schemes are able to capture the additional dispersive effects even on the coarser mesh. We
 229 also note that fourth-order schemes are more effective in capturing these effects compared to the third-
 230 order scheme. Furthermore, the third-order schemes (**O3-ES-Exp** and **O3-ES-IMEX**) have similar
 231 performance, and similarly, the fourth-order schemes (**O4-ES-Exp** and **O4-ES-IMEX**) have similar
 232 performance.

233 We can also observe this from the time evolution of total entropy in the domain for ion flow in
 234 Figure (1(c)) and electron flow in Figure (1(d)). We note that the same order schemes have almost the
 235 same entropy decay behaviour. Furthermore, third and fourth-order schemes have smaller entropy dissi-
 236 pation compared to the second-order schemes, while fourth-order schemes have less entropy dissipation
 237 compared to third-order schemes.

	$r_i = -r_e = 10^4/\sqrt{4\pi}$				$r_i = -r_e = 10^5/\sqrt{4\pi}$			
Number of cells	100	200	400	800	100	200	400	800
O2-ES-Exp	3.24s	5.34s	9.80s	17.90s	85.68s	133.99s	228.22s	413.55s
O2-ES-IMEX	0.49s	1.30s	4.25s	14.28s	0.50s	1.22s	3.70s	12.11s
O3-ES-Exp	2.23s	3.83s	6.94s	13.04s	32.88s	53.33s	96.31s	182.08s
O3-ES-IMEX	0.72s	2.02s	6.31s	22.14s	0.97s	2.69s	8.51s	30.01s
O4-ES-Exp	6.03s	10.72s	20.01s	37.98s	61.96s	108.51s	198.32s	374.54s
O4-ES-IMEX	1.30s	3.78s	12.86s	44.90s	1.27s	3.82s	12.87s	47.00s

Table 4: **Relativistic Brio–Wu test problem with finite plasma skin depth**: Computational times using $r_i = -r_e = 10^4/\sqrt{4\pi}$ and $r_i = -r_e = 10^5/\sqrt{4\pi}$ for the second (**O2-ES-Exp** and **O2-ES-IMEX**), third (**O3-ES-Exp** and **O3-ES-IMEX**), and fourth (**O4-ES-Exp** and **O4-ES-IMEX**) order schemes.

238 We also consider the stiff source terms with $r_i = -r_e = 10^4/\sqrt{4\pi}$ and $r_i = -r_e = 10^5/\sqrt{4\pi}$ leading to
 239 very small plasma skin depth, which will require substantially more cells to resolve the dispersive effects.
 240 In Figure (2), we show solutions obtained from different schemes using 400 cells. For both the values
 241 of r_i , all the schemes produce solutions close to RMHD solution, with third and fourth-order schemes
 242 performing better than the second-order schemes. Also, there is no visible difference in Explicit and
 243 IMEX scheme of same order. To further show the effects of higher values of r_i , in Figure (2(c)), we show
 244 solutions using **O4-ES-IMEX** scheme on 400 cells, for different values of r_i . For $r_i = 10^3/\sqrt{4\pi}$, we can
 245 see the dispersive effects are resolved. However, for $r_i = 10^4/\sqrt{4\pi}$ and $r_i = 10^5/\sqrt{4\pi}$, the scheme was
 246 not able to resolve the small scale oscillation; nevertheless, the scheme produces a stable solution thanks
 247 to the built in entropy stability property of the scheme.

248 To demonstrate the effectiveness of ARK-IMEX schemes over the explicit schemes for the stiff source
 249 terms, in Table (4), we present the computational time for the cases $r_i = -r_e = 10^4/\sqrt{4\pi}$ and $r_i =$
 250 $-r_e = 10^5/\sqrt{4\pi}$ on 100, 200, 400, and 800 cells. We use the MPI-parallelized code on a CPU with 10
 251 cores. At the lower resolutions, the source terms will govern the time step as time step given by the CFL
 252 restriction is large. Hence, we observe consistently that IMEX schemes outperform the explicit schemes
 253 on the coarser mesh. In the case of $r_i = -r_e = 10^4/\sqrt{4\pi}$, we see that IMEX outperform the explicit
 254 schemes up to 400 cells. On 800 cells, we observe that the IMEX schemes are more expensive than the
 255 explicit schemes as at this resolution, stable time step is governed by the CFL condition, not the source
 256 terms. In the case of $r_i = -r_e = 10^5/\sqrt{4\pi}$, we observe that IMEX schemes consistently outperform
 257 explicit scheme even on 800 cells as the stiffness in the source is very strong and hence it decides the
 258 stable time step for explicit schemes.

259 Given the similar accuracy of the explicit and IMEX schemes of the same order, and the ability
 260 of IMEX schemes to overcome time-step restriction due to stiff source terms, especially at the lower
 261 resolutions, in the remaining test cases, we will present numerical results only for the ARK-IMEX
 262 schemes. We have also computed the results using explicit schemes (whenever source terms are not stiff)
 263 also, and the solutions are similar to those of the IMEX schemes of the same order.

264 6.1.3 Self-similar current sheet with finite resistivity

265 The test case was first considered in [10], and the two-fluid relativistic extension is presented in [12],
 266 which is used here. We consider the modified Equations (27a) and (27b) to capture the resistive effects.

For resistive RMHD solution [10], only the B_y -component has non-zero variation, whose time evolution includes the resistive effects and is governed by the diffusion equation,

$$\frac{\partial B_y}{\partial t} - D \frac{\partial^2 B_y}{\partial x^2} = 0. \quad (30)$$

The relation between the diffusion coefficient and resistivity constant is given by the expression $D = \eta c^2$. An exact self similar solution of Eqn. (30) in the resistive RMHD regime [10] is given by

$$B_y(x, t) = B_0 \operatorname{erf}\left(\frac{x}{2\sqrt{Dt}}\right), \quad (31)$$

267 where “erf” is the error function.

For two-fluid relativistic plasma equations, we consider the initial B_y at the time $t = 1.0$, using $B_0 = 1.0$ and $\eta c^2 = 0.01$. The domain is $[-1.5, 1.5]$ with Neumann boundary conditions. The charge to mass ratios are $r_i = -r_e = 10^3$, the ion and electron density are 0.5, and the ion and electron pressures are 25.0. The z -component of the ion and electron velocity is given by

$$u_{z_i} = -u_{z_e} = \frac{B_0}{r_i \rho_i \sqrt{\pi D}} \exp\left(-\frac{x^2}{4D}\right).$$

268 All other variables are set to zero. We evolve the solution from the initial time $t = 1.0$ to final time $t = 9.0$
 269 using ARK-IMEX schemes **O2-ES-IMEX**, **O3-ES-IMEX** and **O4-ES-IMEX**, and the solutions using
 270 400 cells are shown in Figure (3). We observe that, in the presence of friction terms as in Eqn. (27a), (27b),
 271 the obtained B_y profile for all the schemes agrees with the resistive RMHD analytical expression (31).
 272 Furthermore, all the schemes are highly accurate and there is no visible difference in the solution profiles.

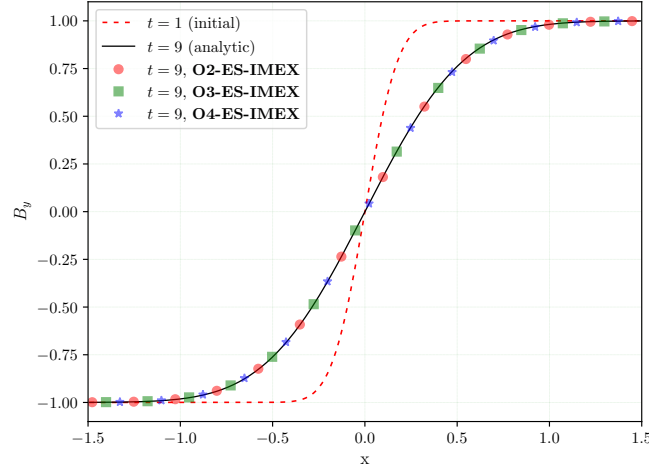


Figure 3: **Self-similar current sheet with finite resistivity**: Comparison of the B_y profile for ARK-IMEX schemes (**O2-ES-IMEX**, **O3-ES-IMEX**, and **O4-ES-IMEX**) using 400 cells.

273 6.2 Two-dimensional test cases

For two-dimensional test cases, the time step is chosen using,

$$\Delta t = \text{CFL} \cdot \min \left\{ \left(\frac{\Delta x}{\Lambda_{max}^x(\mathbf{U}_{i,j})} + \frac{\Delta y}{\Lambda_{max}^y(\mathbf{U}_{i,j})} \right) : 1 \leq i \leq N_x, 1 \leq j \leq N_y \right\}$$

274 where $\Lambda_{max}^x(\mathbf{U}_{i,j}) = \max\{|\Lambda_k^x(\mathbf{U}_{i,j})|: 1 \leq k \leq 18\}$ and $\Lambda_{max}^y(\mathbf{U}_{i,j}) = \max\{|\Lambda_k^y(\mathbf{U}_{i,j})|: 1 \leq k \leq 18\}$. We
 275 take CFL to be 0.45 and present the numerical results for the ARK-IMEX schemes (**O3-ES-IMEX**,
 276 and **O4-ES-IMEX**). We have not presented the results for second-order scheme **O2-ES-IMEX** as the
 277 scheme is less accurate when compared to the third and fourth order schemes.

To monitor the divergence of magnetic field, we also plot the evolution of the L^1 -norm of $\nabla \cdot \mathbf{B}$, which is calculated as,

$$\Delta x \Delta y \sum_{i=1}^{N_x} \sum_{j=1}^{N_y} |(\nabla \cdot \mathbf{B})_{i,j}| \quad (32)$$

where $(\nabla \cdot \mathbf{B})_{i,j}$ is evaluated using the central difference approximation in each direction, i.e.

$$(\nabla \cdot \mathbf{B})_{i,j} := \frac{B_{x,i+1,j} - B_{x,i-1,j}}{2\Delta x} + \frac{B_{y,i,j+1} - B_{y,i,j-1}}{2\Delta y}. \quad (33)$$

278

279 6.2.1 Relativistic Orzag-Tang test case

Orzag-Tang test case was first proposed for the non-relativistic MHD systems in [48]. Here, we consider the two-fluid relativistic extension of the test case, presented in [29]. To have consistent comparison with the results in [29], we consider the Maxwell's equations with scaled source (29). The computational domain is $[0.0, 1.0] \times [0.0, 1.0]$ with periodic boundary conditions, and the initial conditions are given by,

$$\begin{pmatrix} \rho_i \\ u_{x_i} \\ u_{y_i} \\ p_i \end{pmatrix} = \begin{pmatrix} \frac{25}{72\pi} \\ -\frac{\sin(2\pi y)}{2} \\ \frac{\sin(2\pi x)}{2} \\ \frac{5}{24\pi} \end{pmatrix}, \quad \begin{pmatrix} \rho_e \\ u_{x_e} \\ u_{y_e} \\ p_e \end{pmatrix} = \begin{pmatrix} \frac{25}{72\pi} \\ -\frac{\sin(2\pi y)}{2} \\ \frac{\sin(2\pi x)}{2} \\ \frac{5}{24\pi} \end{pmatrix}, \quad \begin{pmatrix} B_x \\ B_y \end{pmatrix} = \begin{pmatrix} -\sin(2\pi y) \\ \sin(4\pi x) \end{pmatrix}$$

280 The initial electric field is $-\mathbf{u}_i \times \mathbf{B}$ and all other variables are set to zero. We use the charge to mass
 281 ratios of $r_i = -r_e = 10^3/\sqrt{4\pi}$, thus the plasma skin depth approximates to 3.0×10^{-3} . We choose
 282 adiabatic indices $\gamma_i = \gamma_e = 5/3$ and simulate till time $t = 1.0$ on a mesh with 200×200 cells.

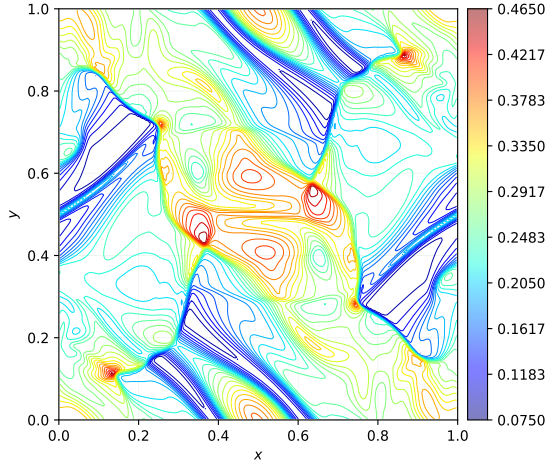
283 Figure (4) and (5) show the total density, total pressure, ion Lorentz factor and magnitude of the
 284 magnetic field for **O3-ES-IMEX** and **O4-ES-IMEX** schemes, respectively. The results for both the
 285 schemes are comparable to those in [29], and both the schemes have similar performance. As the cell
 286 size is higher than the plasma skin depth, the solution is comparable to those of the RMHD case.

287 Figure (6) shows the time evolution of the total fluid entropy $\mathcal{U}_i + \mathcal{U}_e$ for **O3-ES-IMEX** and **O4-**
 288 **ES-IMEX** schemes. Initially, we do not see significant decay as discontinuities are not present in the
 289 solution. However, at time approximately $t = 0.4$, the solutions start to develop discontinuities and we
 290 see sharp decay in the entropy. We also observe that the third-order scheme decays slightly more entropy
 291 than the fourth-order scheme, however, the difference is very small.

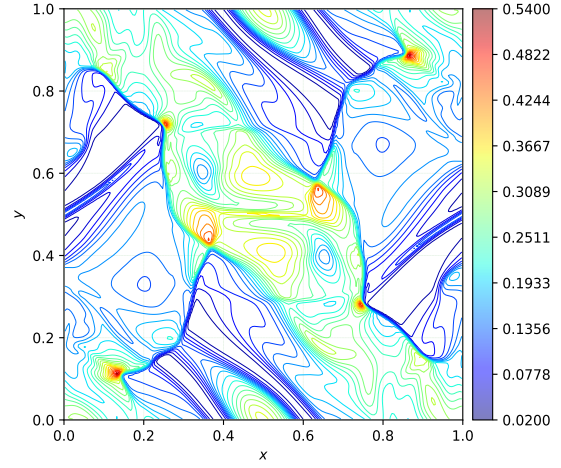
292 In Figs. 7(a) and 7(b), we have plotted the absolute value of the undivided divergence of the mag-
 293 netic field, i.e., $|2\Delta x(\nabla \cdot \mathbf{B})_{i,j}|$ (Note that $\Delta x = \Delta y$) for **O3-ES-IMEX** and **O4-ES-IMEX** schemes,
 294 respectively [29]. We observe the highest values of the divergence error correlate with the location of the
 295 discontinuities in the solutions. Furthermore, both schemes have similar absolute maximum errors. To
 296 observe the long-time behavior of the divergence errors, in Fig. 7(c), we have plotted the time evolution
 297 of L^1 -norm of divergence of \mathbf{B} for both the schemes till time $t = 2$. We observe that both schemes have
 298 similar L^1 errors.

299 6.2.2 Relativistic two-fluid blast problem

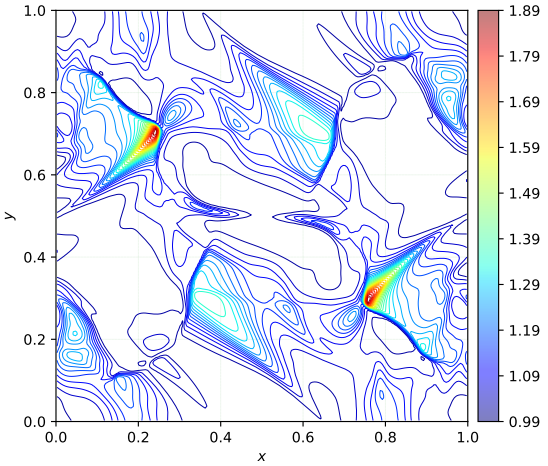
300 We consider the two-fluid relativistic extension of the strong cylindrical RMHD explosion described in [6].
 301 We follow [12, 29] to consider a computational domain of $[-6, 6] \times [-6, 6]$ with Neumann boundary
 302 conditions. To describe the initial fluid profile, consider $\rho_{in} = 10^{-2}$, $p_{in} = 1.0$, $\rho_{out} = 10^{-4}$ and
 303 $p_{out} = 5 \times 10^{-4}$. Also, let us denote the radial distance $r = \sqrt{x^2 + y^2}$ from the center of the computational
 304 domain. Inside the disc of radius 0.8, i.e., $r < 0.8$, we define the densities $\rho_i = \rho_e = 0.5 \times \rho_{in}$ and the



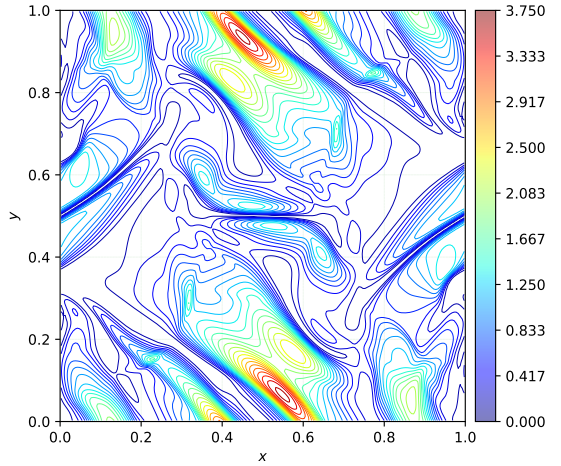
(a) Plot of total density $\rho_i + \rho_e$.



(b) Plot of total pressure $p_i + p_e$.

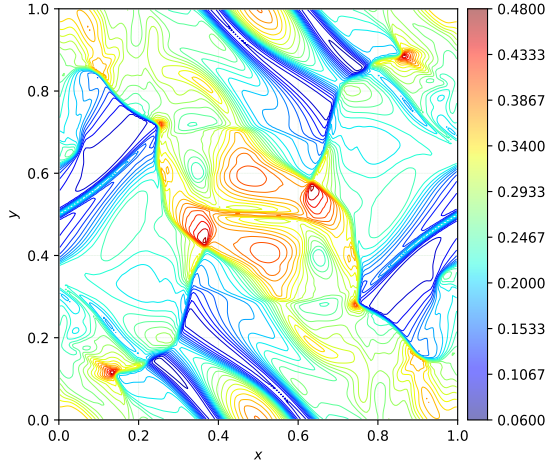


(c) Plot of ion Lorentz factor Γ_i .

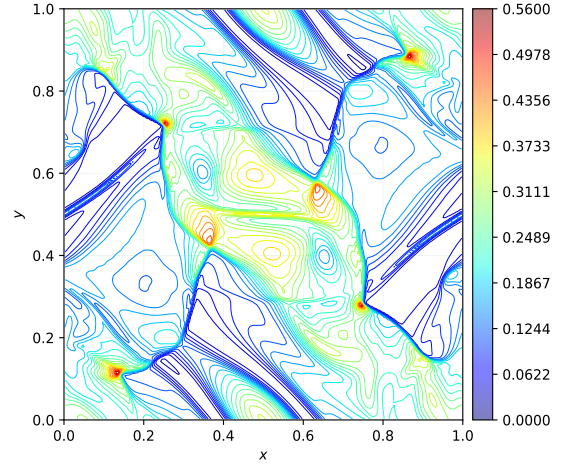


(d) Plot of magnitude of the Magnetic field, $\frac{|\mathbf{B}|^2}{2}$.

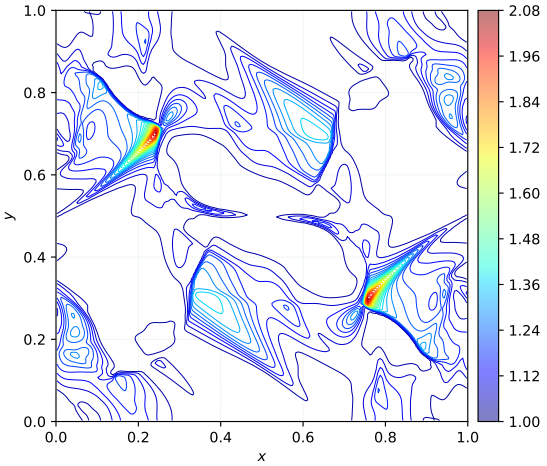
Figure 4: **Relativistic Orzag-Tang test case**: Plots of total density, total pressure, Ion Lorentz factor, and magnitude of magnetic field $\frac{|\mathbf{B}|^2}{2}$ using **O3-ES-IMEX** scheme and 200×200 cells at time $t = 1.0$. We have plotted 30 contours for each variable.



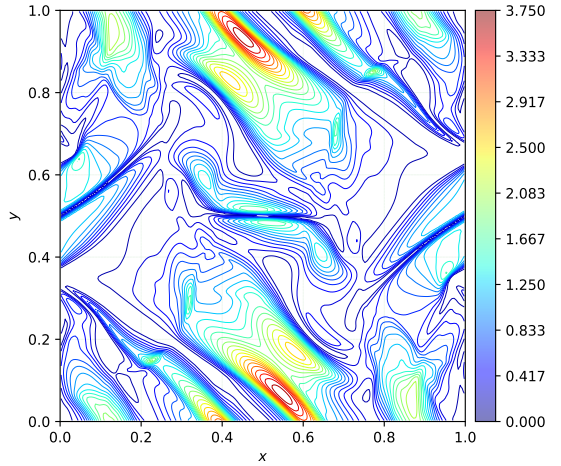
(a) Plot of total density $\rho_i + \rho_e$.



(b) Plot of total pressure $p_i + p_e$.



(c) Plot of ion Lorentz factor Γ_i .



(d) Plot of magnitude of the Magnetic field, $\frac{|\mathbf{B}|^2}{2}$.

Figure 5: **Relativistic Orzag-Tang test case**: Plots of total density, total pressure, Ion Lorentz factor, and magnitude of magnetic field $\frac{|\mathbf{B}|^2}{2}$ using **O4-ES-IMEX** scheme and 200×200 cells at time $t = 1.0$. We have plotted 30 contours for each variable.

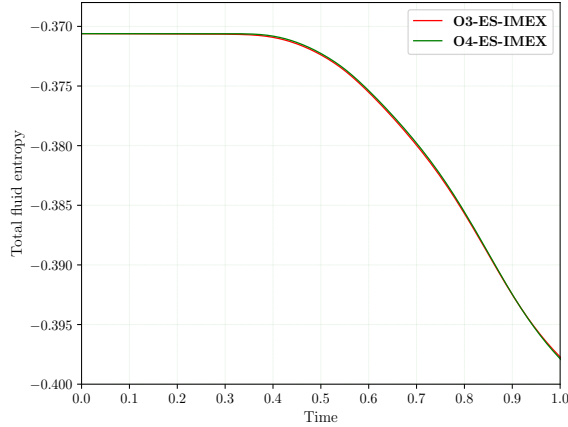


Figure 6: **Relativistic Orzag-Tang test case**: Total fluid entropy $\mathcal{U}_i + \mathcal{U}_e$ evolution for the schemes **ES-O3-IMEX** and **ES-O4-IMEX**.

305 pressures $p_i = p_e = 0.5 \times p_{in}$. Also, outside the disc of radius 1.0, i.e., $r > 1$, we define the densities
 306 $\rho_i = \rho_e = 0.5 \times \rho_{out}$ and the pressures $p_i = p_e = 0.5 \times p_{out}$. In the range $0.8 \leq r \leq 1.0$, the densities
 307 and pressures are defined using a linear profile, such that the densities and the pressures decreases with
 308 increase in the radius r and at the boundaries $r = 0.8$ and $r = 1.0$ they matches the prescribed constant
 309 states. The magnetic field has been initialized in the x -direction only, as $B_x = B_0$. We set all remaining
 310 variables to zero. The charge to mass ratios are taken to be $r_i = -r_e = 10^3$ and $\gamma_i = \gamma_e = 4/3$.

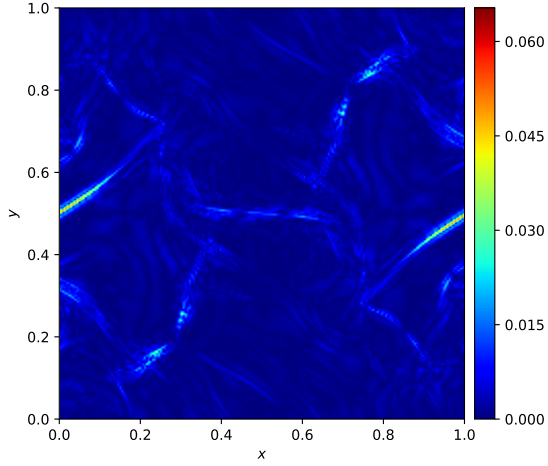
311 The solutions are computed on a mesh of 200×200 cells using the **O3-ES-IMEX** and **O4-ES-**
 312 **IMEX** schemes till final time $t = 4.0$. We consider two values of parameter B_0 , such that $B_0 = 0.1$
 313 denoting the case of the weakly magnetized medium, and $B_0 = 1.0$ denoting the case of the strongly
 314 magnetized medium. In Figures (8) and (9), we plot the results for weakly magnetized medium for
 315 **O3-ES-IMEX** and **O4-ES-IMEX** schemes, respectively. The figures show the log to the base 10 of
 316 total density and total pressure; we also plot the ion Lorentz factor and magnitude of the magnetic
 317 field. It can be observed that both the schemes produce stable results and are able to capture the waves
 318 accurately. Furthermore, the results are comparable to those in [12] and [29].

319 Similarly, in the case of strongly magnetized medium we plot the results for **O3-ES-IMEX** and
 320 **O4-ES-IMEX** schemes in Figures (10) and (11), respectively. We observe a substantial change in the
 321 solution profile. Again both the schemes are able to capture the blast waves accurately.

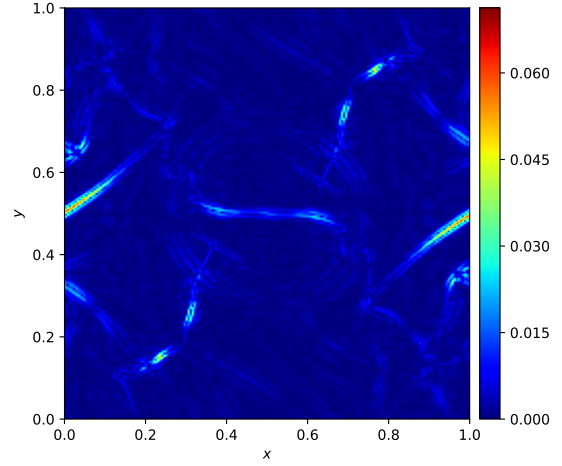
322 In Figure (12), we plot the evolution of the total fluid entropy $\mathcal{U}_i + \mathcal{U}_e$ for the **O3-ES-IMEX** and
 323 **O4-ES-IMEX** schemes in weakly and strongly magnetized mediums. As the solutions contain many
 324 discontinuities, we see a strong decay in the entropies. Furthermore, **O4-ES-IMEX** scheme decays less
 325 entropy than the **O3-ES-IMEX** scheme.

326 In Fig. 13 we have presented results for errors in the divergence of the magnetic field. In Figs. 13(a)
 327 and 13(b), we plot the absolute value of undivided divergence of the magnetic field for $B_0 = 0.1$ using
 328 **O3-ES-IMEX** and **O4-ES-IMEX** schemes, respectively [29]. For both schemes, we note that the errors
 329 are well-controlled and concentrated where we have steep gradients in the flows. Furthermore, the errors
 330 for **O3-ES-IMEX** are more spread out than the **O4-ES-IMEX** scheme. In Fig. 13(c), we have plotted
 331 the time evolution of the L^1 -norm of the divergence for $B_0 = 0.1$ using both schemes. We note that the
 332 errors stay relatively small for both the schemes.

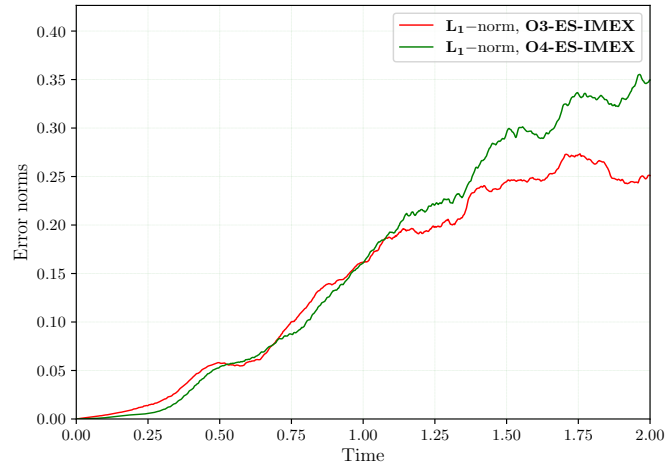
333 In Figs. 13(d) and 13(e), we plot the absolute value of undivided divergence of magnetic field for
 334 $B_0 = 1.0$ using **O3-ES-IMEX** and **O4-ES-IMEX** schemes, respectively [29]. We observe that the
 335 errors for the **O3-ES-IMEX** schemes are much more spread out when compared with the **O4-ES-**
 336 **IMEX** scheme. This can also be observed from Fig. 13(f), where we plot the time evolution of the
 337 L^1 -norm of divergence of the magnetic field. We note that **O4-ES-IMEX** scheme outperforms **O3-ES-**
 338 **IMEX** scheme.



(a) Plot of $|2\Delta x(\nabla \cdot \mathbf{B})_{i,j}|$ using the **O3-ES-IMEX** scheme at time $t = 1.0$.



(b) Plot of $|2\Delta x(\nabla \cdot \mathbf{B})_{i,j}|$ using the **O4-ES-IMEX** scheme at time $t = 1.0$.



(c) Time evolution of L^1 -norms of divergence of \mathbf{B} till time $t = 2.0$ for **O3-ES-IMEX** and **O4-ES-IMEX** schemes.

Figure 7: **Relativistic Orzag-Tang test case**: Plots of the $(|2\Delta x(\nabla \cdot \mathbf{B})_{i,j}|)$ and time evolution of L^1 -norm of divergence of \mathbf{B} for **O3-ES-IMEX** and **O4-ES-IMEX** schemes using 200×200 cells.

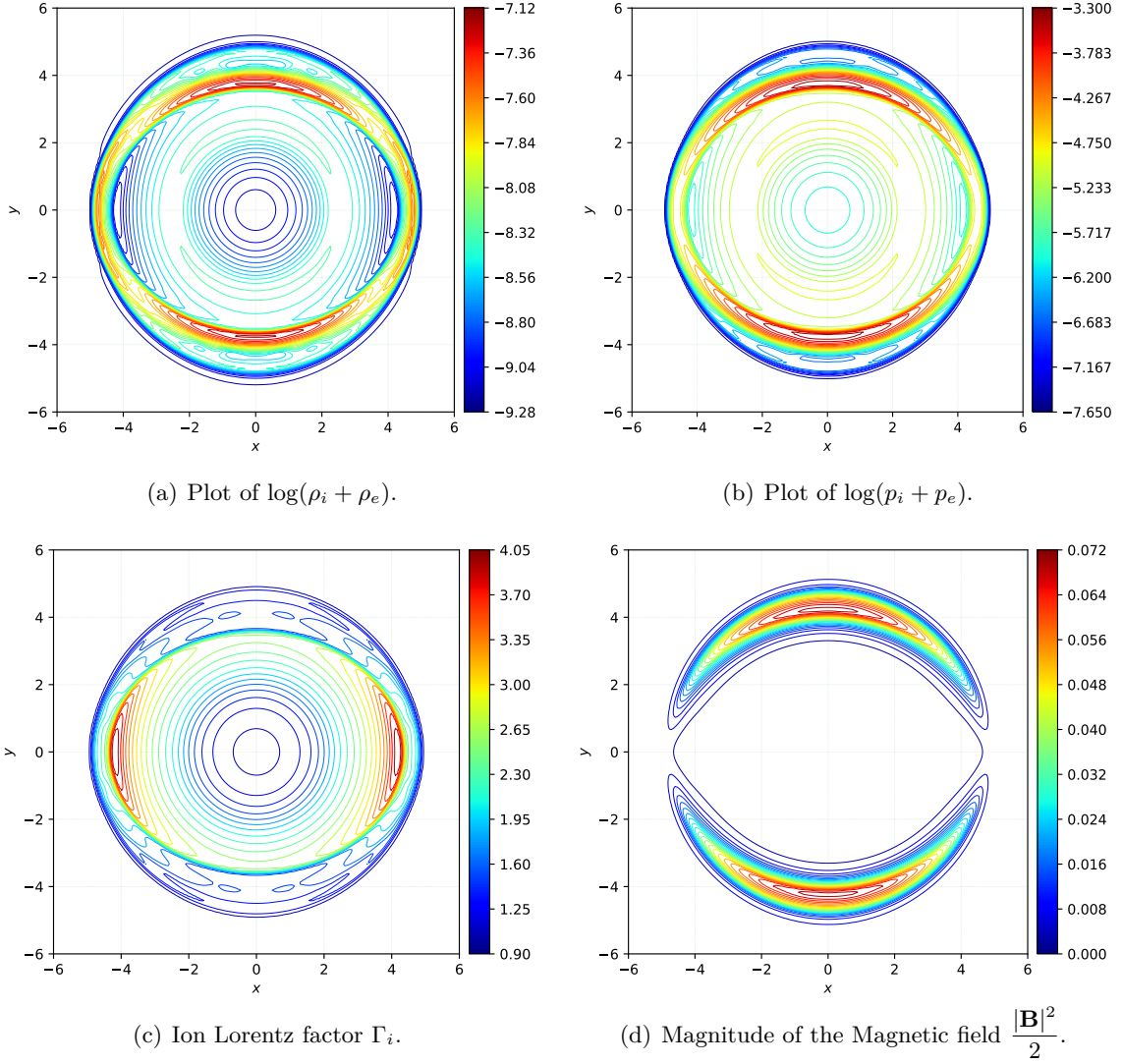
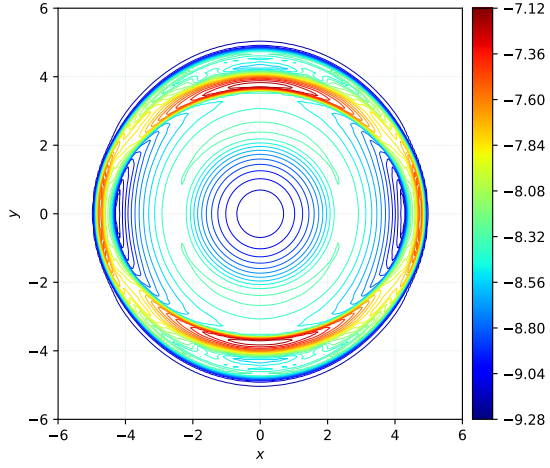
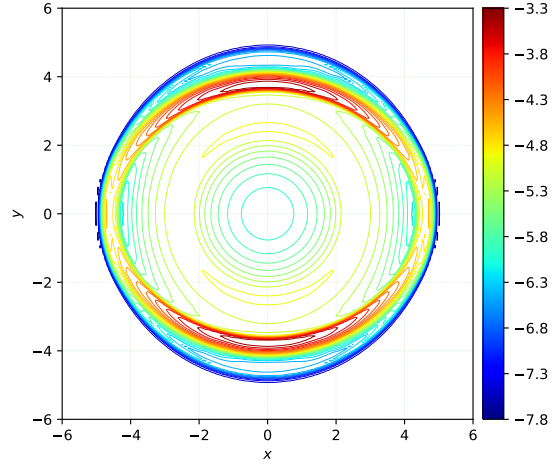


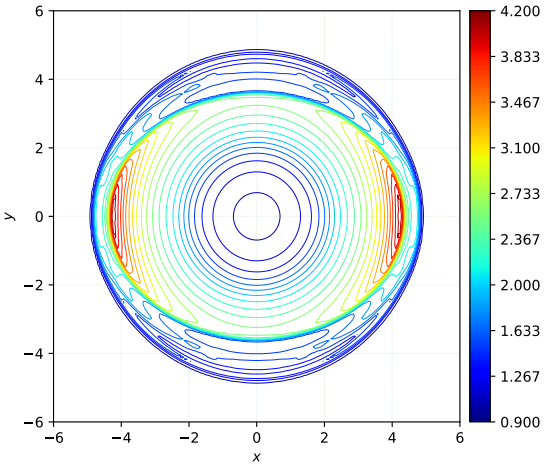
Figure 8: **Relativistic two-fluid blast problem**: Plot for the weakly magnetized medium $B_0 = 0.1$, using **O3-ES-IMEX** scheme with 200×200 cells. We have plotted 30 contours for each variable.



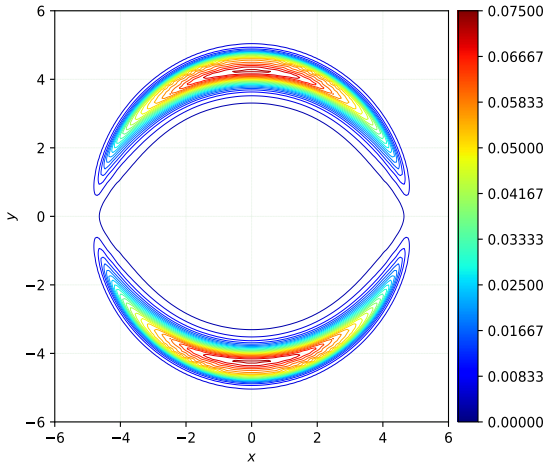
(a) Plot of $\log(\rho_i + \rho_e)$.



(b) Plot of $\log(p_i + p_e)$.

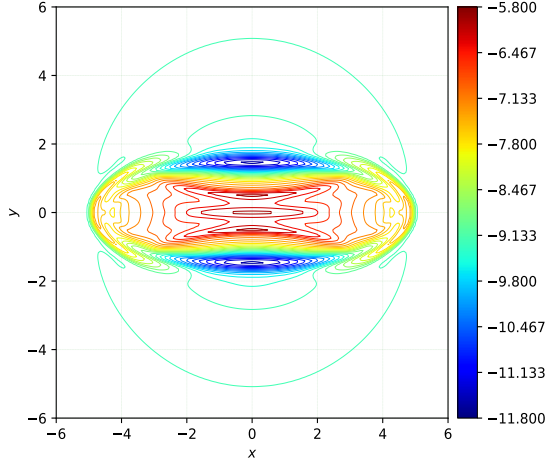


(c) Plot of ion Lorentz factor Γ_i .

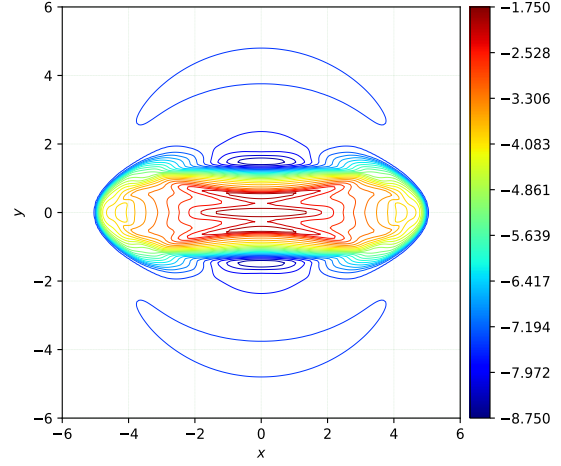


(d) Plot of magnitude of the Magnetic field $\frac{|\mathbf{B}|^2}{2}$.

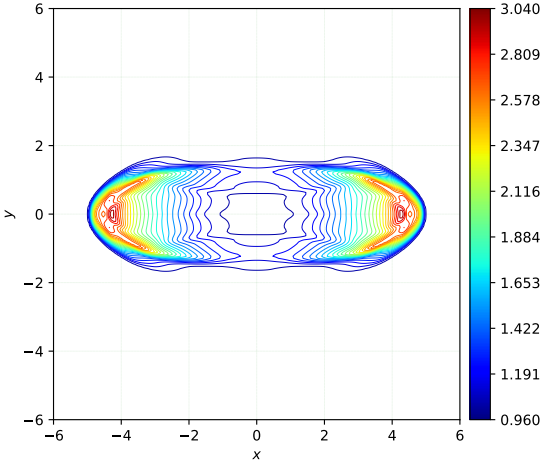
Figure 9: **Relativistic two-fluid blast problem**: Plot for the weakly magnetized medium $B_0 = 0.1$, using **O4-ES-IMEX** scheme with 200×200 cells. We have plotted 30 contours for each variable.



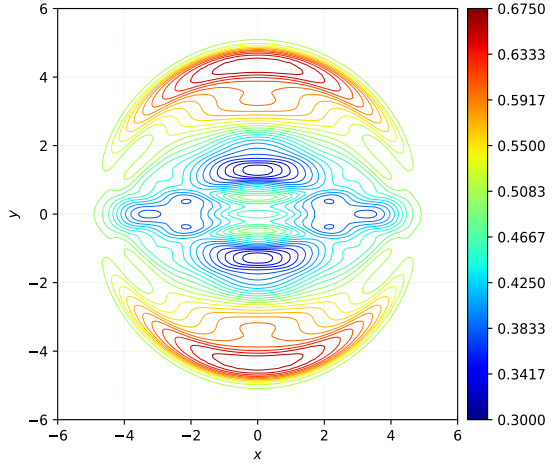
(a) Plot of $\log(\rho_i + \rho_e)$.



(b) Plot of $\log(p_i + p_e)$.

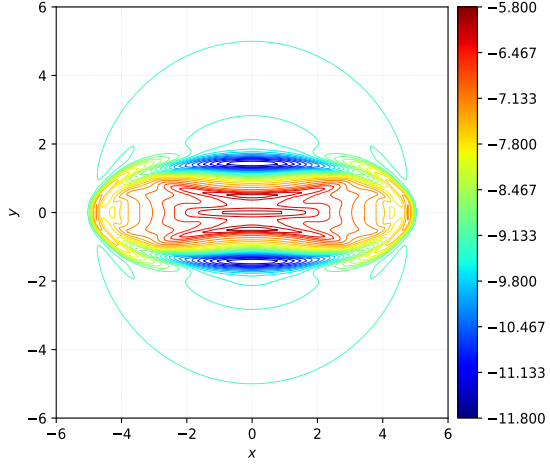


(c) Plot of ion Lorentz factor Γ_i .

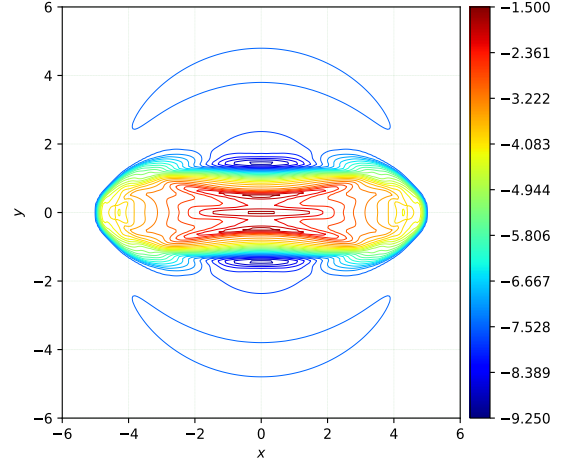


(d) Plot of magnitude of the Magnetic field $\frac{|\mathbf{B}|^2}{2}$.

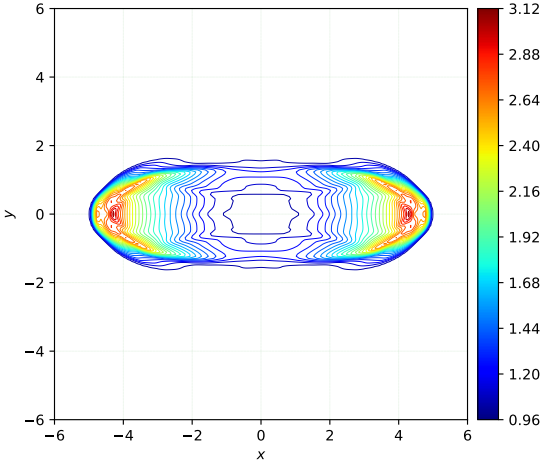
Figure 10: **Relativistic two-fluid blast problem**: Plot for the strongly magnetized medium $B_0 = 1.0$, using **O3-ES-IMEX** scheme with 200×200 cells. We have plotted 30 contours for each variable.



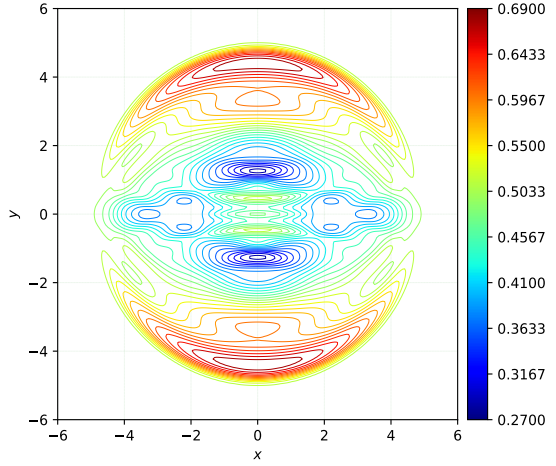
(a) Plot of $\log(\rho_i + \rho_e)$.



(b) Plot of $\log(p_i + p_e)$.

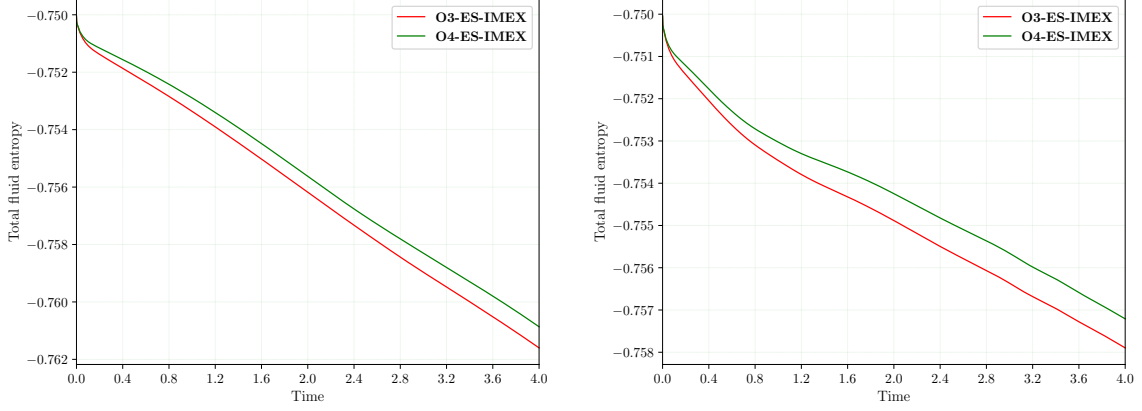


(c) Plot of ion Lorentz factor Γ_i .



(d) Plot magnitude of the Magnetic field $\frac{|\mathbf{B}|^2}{2}$.

Figure 11: **Relativistic two-fluid blast problem**: Plot for the strongly magnetized medium $B_0 = 1.0$, using **O4-ES-IMEX** scheme with 200×200 cells. We have plotted 30 contours for each variable.



(a) Total entropy fluid decay for weakly magnetized medium, $B_0 = 0.1$. (b) Total fluid entropy decay for strongly magnetized medium, $B_0 = 1.0$.

Figure 12: **Relativistic two-fluid blast problem**: Total fluid entropy $\mathcal{U}_i + \mathcal{U}_e$ evolution of the schemes **ES-O3-IMEX** and **ES-O4-IMEX** for the weakly and strongly magnetized medium.

339 6.2.3 Relativistic two-fluid GEM challenge problem

In this test, we consider two-fluid relativistic Geospace Environment Modeling (GEM) magnetic reconnection problem from [12], which is an extension of the non-relativistic GEM magnetic reconnection problem given in [49]. We consider the modified Equations (27a) and (27b) to capture the resistive effects. The computational domain is $[-L_x/2, L_x/2] \times [-L_y/2, L_y/2]$ where $L_x = 8\pi$ and $L_y = 4\pi$, with periodic boundary conditions at $x = \pm L_x/2$ and conducting wall boundary at $y = \pm L_y/2$ boundary. The ion-electron mass ratio is taken to be $m_i/m_e = 25$ with $m_i = 1$. Accordingly, we have $r_i = 1.0$ and $r_e = -25.0$. The unperturbed x -component of the magnetic field is taken to be $B_x(y) = B_0 \tan(y/d)$ with $B_0 = 1.0$, where $d = 1.0$ is the thickness of the current sheet. On the other hand, unperturbed y - and z -components of the magnetic field are assumed to be zero. After the perturbation, the initial conditions become

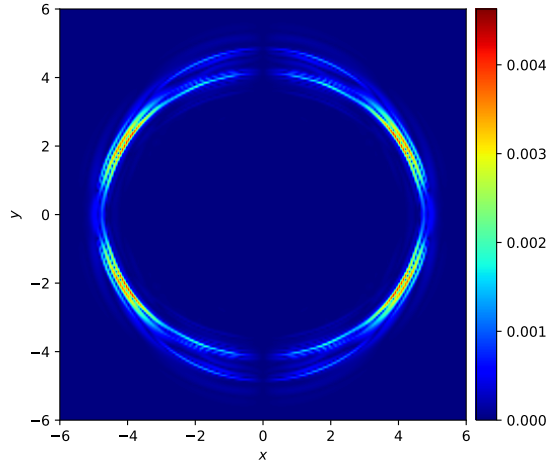
$$\begin{pmatrix} \rho_i \\ u_{z_i} \\ p_i \\ \rho_e \\ u_{z_e} \\ p_e \\ B_x \\ B_y \end{pmatrix} = \begin{pmatrix} n \\ \frac{c}{2d} B_0 \operatorname{sech}^2(y/d) \\ 0.2 + \frac{B_0^2 \operatorname{sech}^2(y/d)}{4} \frac{5}{24\pi} \\ \frac{m_e}{m_p} n \\ -(u_z)_i \\ -p_i \\ B_0 \tan(y/d) - B_0 \psi_0 \frac{\pi}{L_y} \cos\left(\frac{\pi x}{L_x}\right) \sin\left(\frac{\pi y}{L_y}\right) \\ B_0 \psi_0 \frac{\pi}{L_x} \sin\left(\frac{\pi x}{L_x}\right) \cos\left(\frac{\pi y}{L_y}\right) \end{pmatrix}$$

340 where $n = \operatorname{sech}^2(y/d) + 0.2$. All other variables are set to zero. We set resistivity constant as $\eta = 0.01$,
 341 and adiabatic indices as $\gamma_i = \gamma_e = 4.0/3.0$.

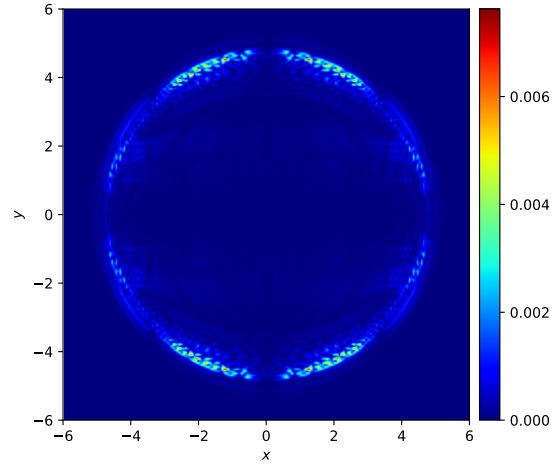
342 Figures (14) to (17) show the total density, z -component of magnetic field, x -component of ion
 343 velocity and x -component of electron velocity on a mesh of 512×256 cells. The plots also contain
 344 field line for (B_x, B_y) . The solution is shown at time $t = 40$ and $t = 80$ using **O3-ES-IMEX** and
 345 **O4-ES-IMEX** schemes. We observe that solutions from both the schemes are similar and agree with
 346 the solutions presented in [12].

Figure (18) shows the time evolution of the reconnected magnetic flux,

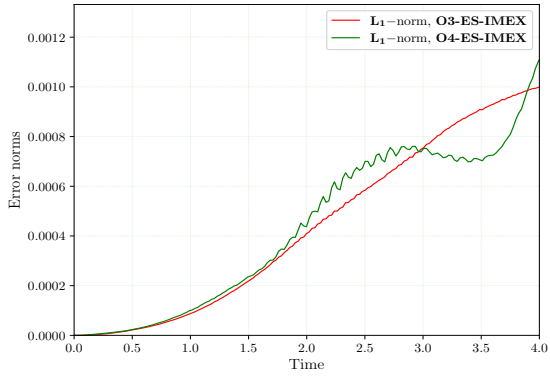
$$\psi(t) = \frac{1}{2B_0} \int_{-L_x/2}^{L_x/2} |B_y(x, y = 0, t)| dx.$$



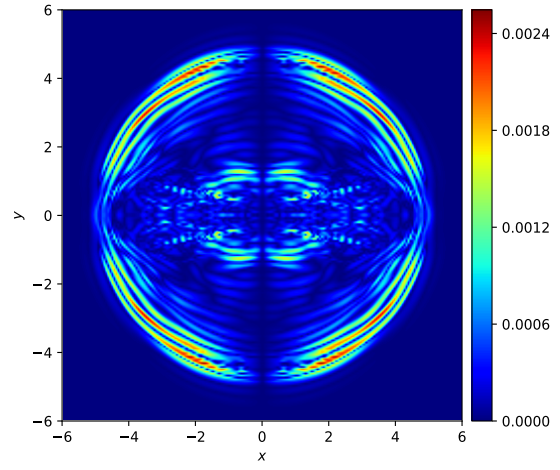
(a) Plot of $|2\Delta x(\nabla \cdot \mathbf{B})_{i,j}|$ for $B_0 = 0.1$ using the **O3-ES-IMEX** scheme at time $t = 4.0$.



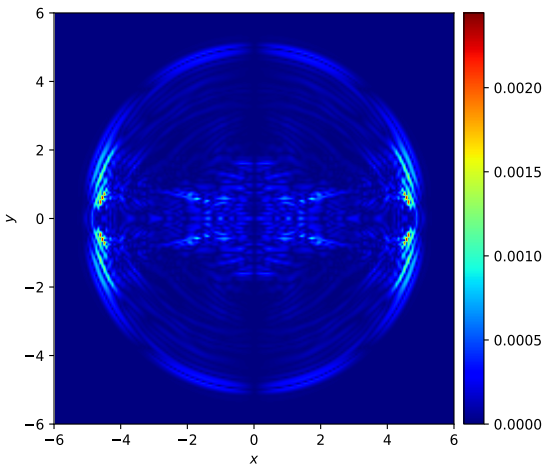
(b) Plot of $|2\Delta x(\nabla \cdot \mathbf{B})_{i,j}|$ for $B_0 = 0.1$ using the **O4-ES-IMEX** scheme at time $t = 4.0$.



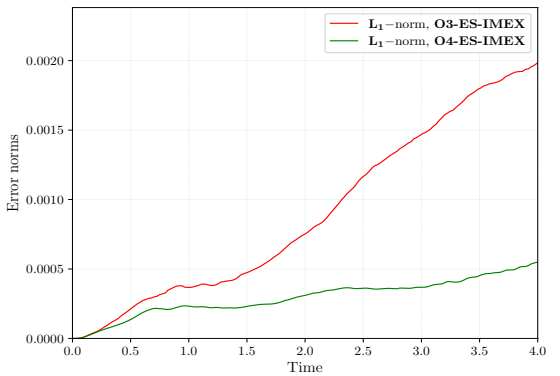
(c) Time evolution of L^1 -norms of divergence of \mathbf{B} for $B_0 = 0.1$ till time $t = 4.0$ using **O3-ES-IMEX** and **O4-ES-IMEX** schemes.



(d) Plot of $|2\Delta x(\nabla \cdot \mathbf{B})_{i,j}|$ for $B_0 = 1.0$ using the **O3-ES-IMEX** scheme at time $t = 4.0$.



(e) Plot of $|2\Delta x(\nabla \cdot \mathbf{B})_{i,j}|$ for $B_0 = 1.0$ using the **O4-ES-IMEX** scheme at time $t = 4.0$.



(f) Time evolution of L^1 -norms of divergence of \mathbf{B} for $B_0 = 1.0$ till time $t = 4.0$ using **O3-ES-IMEX** and **O4-ES-IMEX** schemes.

Figure 13: **Relativistic two-fluid blast problem**: Plots of the $(|2\Delta x(\nabla \cdot \mathbf{B})_{i,j}|)$ and time evolution of L^1 -norms of divergence of \mathbf{B} for $B_0 = 0.1$ and $B_0 = 1.0$ and schemes **O3-ES-IMEX** and **O4-ES-IMEX** using 200×200 cells.

347 at various resolutions. We also compare it with the results presented in [12]. It is observed that both
 348 schemes are able to capture the reconnected flux at various resolutions. Only for times greater than
 349 $t = 80$, we see a difference in the reconnection flux for the different schemes, but at this time, the flow
 350 is already quite turbulent.

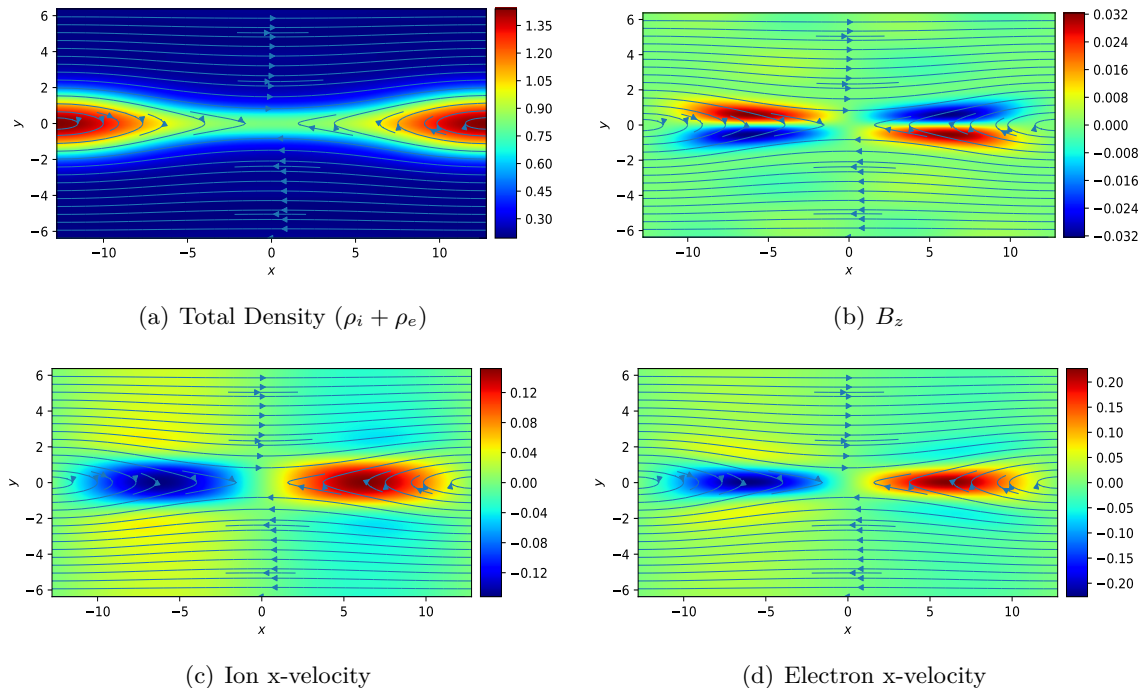


Figure 14: **Relativistic two-fluid GEM challenge problem**: Plots for the total density, B_z -component, Ion x -velocity, and Electron x -velocity on the mesh 512×256 , using scheme **O3-ES-IMEX**, at time $t=40.0$.

351 In Fig. 19, we plot errors for the divergence of the magnetic fields. In Figs. 19(a) and 19(b) we plot the
 352 undivided divergence of magnetic field using **O3-ES-IMEX** and **O4-ES-IMEX** schemes, respectively.
 353 We again observe that the errors are concentrated where flows have strong gradients. Both schemes
 354 have similar errors, with **O3-ES-IMEX** having more spread-out errors. In Fig. 19(c), we plot the time
 355 evolution of the L^1 -norms of divergence of the magnetic field. We again observe that both schemes have
 356 similar L^1 errors.

357 7 Conclusion

358 The two-fluid relativistic plasma flow equations are a multi-physics model that couples relativistic hydro-
 359 dynamic conservation laws with Maxwell's equations. This model is non-linear and exhibits non-smooth
 360 and multi-scale phenomena. In this article, we have designed arbitrary high-order finite-difference en-
 361 tropy stable schemes for the model. This was achieved by exploiting the structure of the flux and by
 362 demonstrating that the source terms do not contribute to the fluid entropies. Furthermore, we have also
 363 presented ARK-IMEX schemes to overcome the time-step restriction imposed by the stiff source terms.
 364 The implicit step in the ARK-IMEX scheme is efficient as it involves solving only one set of nonlinear
 365 equations in each cell and there is no need for any global nonlinear solver.

366 The proposed schemes are applied to various test cases in one and two dimensions. First, we demon-
 367 strate that the proposed schemes have formal order of accuracy. Then we test the schemes on the Brio-Wu
 368 test problem, where we have finite plasma skin depth. We note that the proposed schemes can resolve
 369 the dispersive effects, and higher-order schemes can capture the finite skin depth effects even on coarser
 370 meshes. We also demonstrate that on the coarser meshes with the stiff source terms, IMEX schemes are

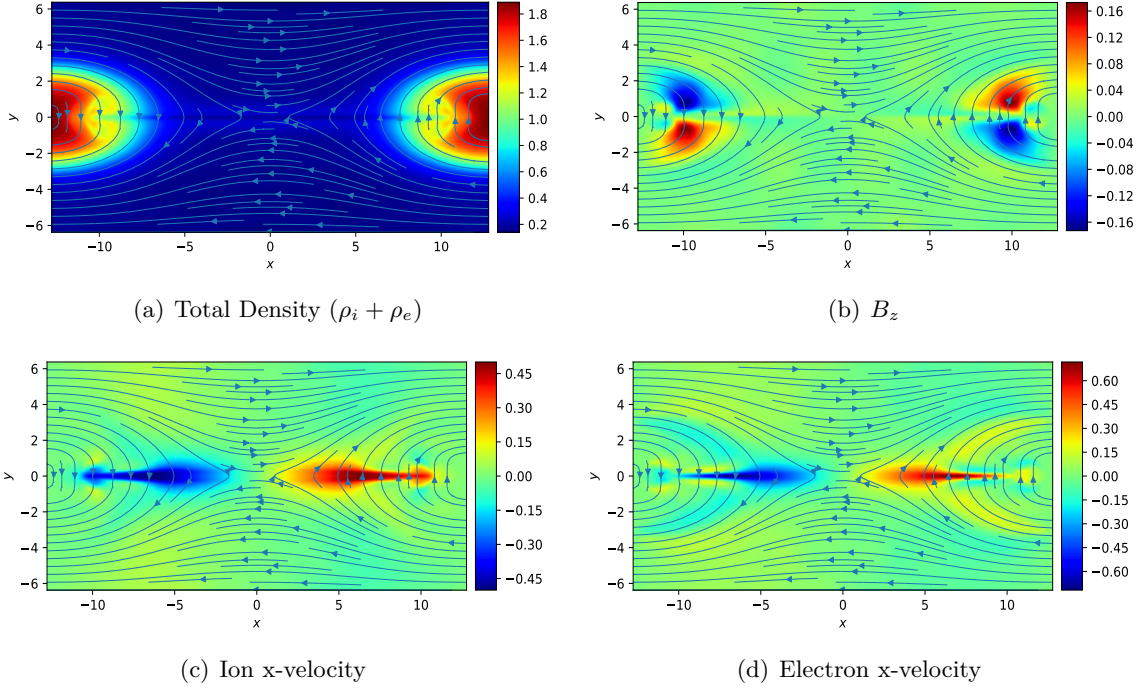


Figure 15: Relativistic two-fluid GEM challenge problem: Plots for the total density, B_z -component, Ion x -velocity, and Electron x -velocity on the mess 512×256 , using scheme **O3-ES-IMEX**, at time $t=80.0$.

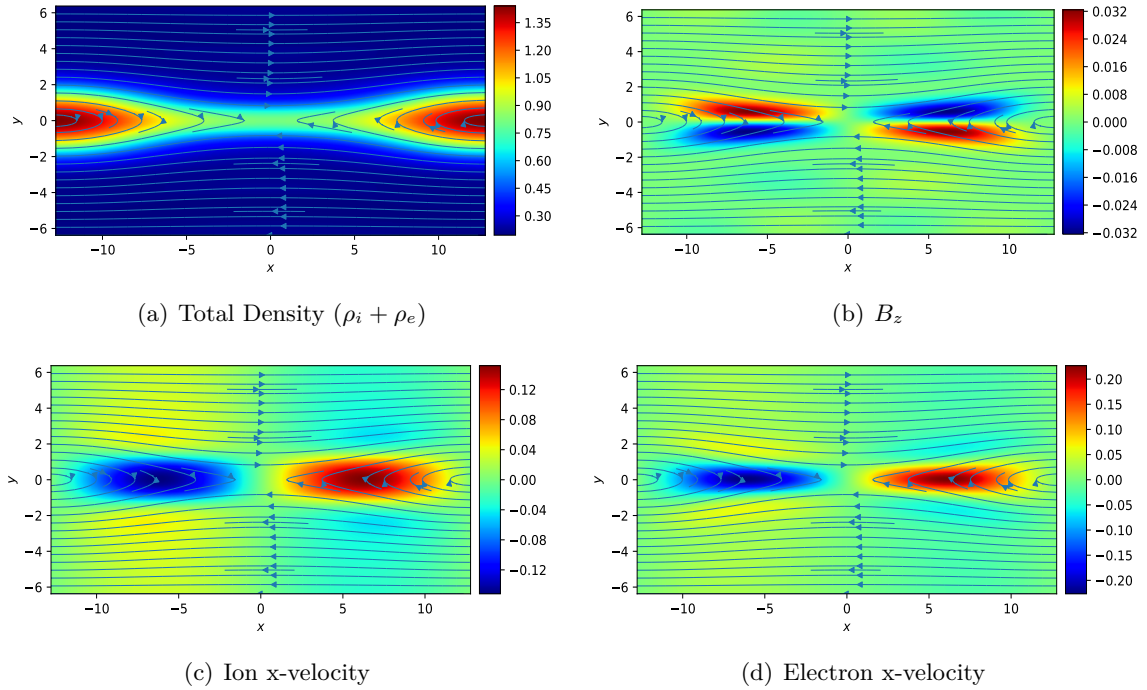


Figure 16: Relativistic two-fluid GEM challenge problem: Plot for the total density, B_z -component, Ion x -velocity, and Electron x -velocity on the mess 512×256 , using scheme **O4-ES-IMEX**, at time $t=40.0$.

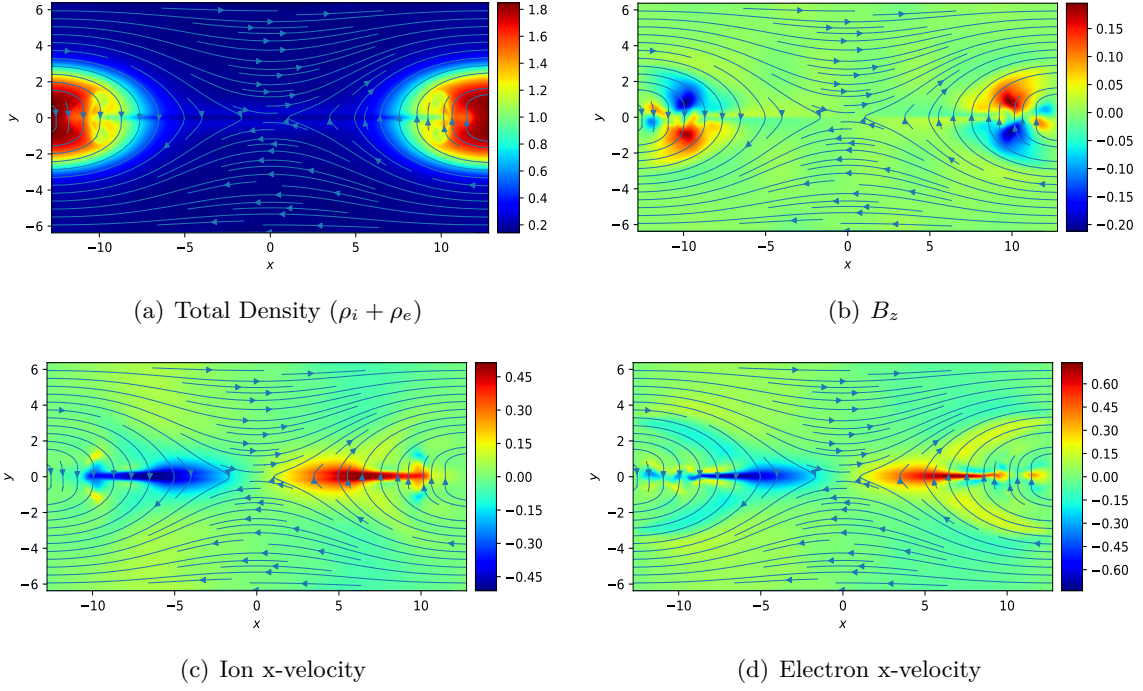


Figure 17: **Relativistic two-fluid GEM challenge problem**: Plot for the total Density, B_z -component, Ion x -velocity, and Electron x -velocity on the mesh 512×256 , using scheme **O4-ES-IMEX**, at time $t=80.0$.

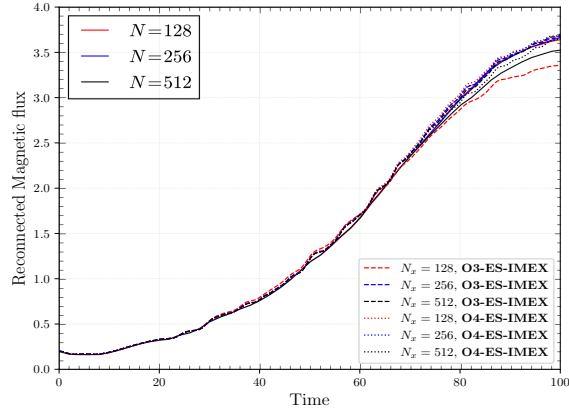
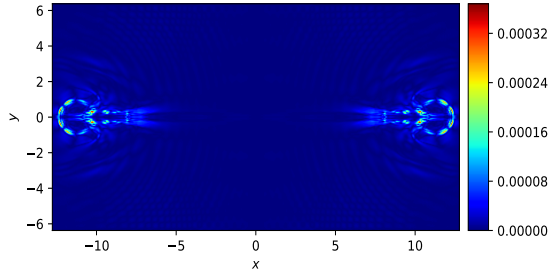
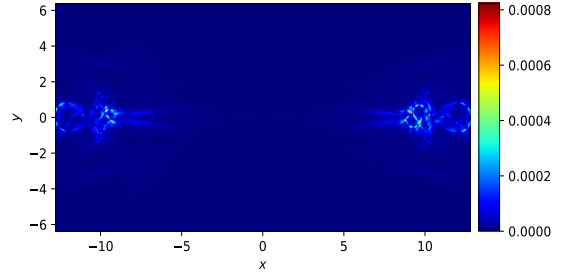


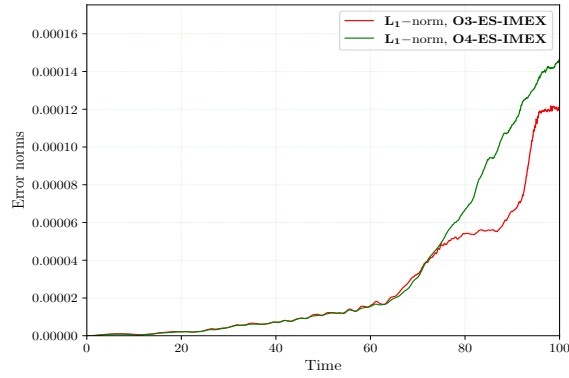
Figure 18: **Relativistic two-fluid GEM challenge problem**: Time development of the reconnected magnetic flux for $N_x = 128, 256, 512$, using schemes **O3-ES-IMEX** and **O4-ES-IMEX**. We overlay the plot on Amano's GEM data [12] (solid lines).



(a) Plot of $|2\Delta x(\nabla \cdot \mathbf{B})_{i,j}|$ using the **O3-ES-IMEX** scheme at time $t = 80.0$.



(b) Plot of $|2\Delta x(\nabla \cdot \mathbf{B})_{i,j}|$ using the **O4-ES-IMEX** scheme at time $t = 80.0$.



(c) Time evolution of L^1 -norms of divergence of \mathbf{B} till time $t = 100.0$ for **O3-ES-IMEX** and **O4-ES-IMEX** schemes.

Figure 19: **Relativistic two-fluid GEM challenge problem**: Plots of the $(|2\Delta x(\nabla \cdot \mathbf{B})_{i,j}|)$ and time evolution of the L^1 -norms of divergence of \mathbf{B} for schemes **O3-ES-IMEX** and **O4-ES-IMEX** schemes using 512×256 cells.

371 more efficient. The SSP-RK and ARK-IMEX schemes have similar accuracy and entropy decay perfor-
372 mance. We then test the scheme on a current sheet problem where resistive effects are considered. We
373 observe that the proposed schemes accurately capture the RMHD solution. We compute the Orzag-Tang
374 vortex problem, blast problem, and GEM challenge problem in two-dimensional test cases. We again
375 show that the schemes are able to capture solution features very well and ensure entropy stability of the
376 solutions. For the GEM problem, the schemes are also able to predict magnetic reconnection flux.

377 Acknowledgments

378 The work of Harish Kumar is supported by VAJRA grant No. VJR/2018/000129 by the Dept. of Science
379 and Technology, Govt. of India. The work of Praveen Chandrashekar was supported by SERB-DST,
380 Govt. of India, under the MATRICS grant No. MTR/2018/000006, and by the Department of Atomic
381 Energy, Government of India, under project no. 12-R&D-TFR-5.01-0520. The authors would also like
382 to thank Prof. Dinshaw Balsara, Univ. of Notre-Dame, USA, for his several suggestions.

383 References

- 384 [1] D. Bhoriya, H. Kumar, Entropy-stable schemes for relativistic hydrodynamics equations, *Zeitschrift*
385 *fur Angewandte Mathematik und Physik* 71 (1) (2020). doi:10.1007/s00033-020-1250-8.
- 386 [2] Y. A. Gallant, J. Arons, Structure of relativistic shocks in pulsar winds: A model of the wisps in
387 the Crab Nebula, *The Astrophysical Journal* 435 (1994) 230. doi:10.1086/174810.
- 388 [3] R. Mochkovitch, V. Maitia, R. Marques, Internal shocks in a relativistic wind as a source for gamma-
389 ray bursts?, *Astrophysics and Space Science* 231 (1-2) (1995) 441–444. doi:10.1007/BF00658666.
- 390 [4] L. D. Landau, E. M. Lifshitz, *Relativistic Fluid Dynamics*, in: *Fluid Mechanics*, Elsevier, 1987, pp.
391 505–514. doi:10.1016/b978-0-08-033933-7.50023-4.
- 392 [5] J. F. Wardle, D. C. Homan, R. Ojha, D. H. Roberts, Electron-positron jets associated with the
393 quasar 3C279, *Nature* 395 (6701) (1998) 457–461. doi:10.1038/26675.
- 394 [6] S. S. Komissarov, A Godunov-type scheme for relativistic magnetohydrodynamics, *Monthly*
395 *Notices of the Royal Astronomical Society* 303 (2) (1999) 343–366. doi:10.1046/j.1365-8711.1999.
396 02244.x.
- 397 [7] D. Balsara, Total Variation Diminishing Scheme for Relativistic Magnetohydrodynamics, *The As-*
398 *trophysical Journal Supplement Series* 132 (1) (2001) 83–101. doi:10.1086/318941.
- 399 [8] L. Del Zanna, N. Bucciantini, P. Londrillo, An efficient shock-capturing central-type scheme for
400 multidimensional relativistic flows II. Magnetohydrodynamics, *Astronomy and Astrophysics* 400 (2)
401 (2003) 397–413. doi:10.1051/0004-6361:20021641.
- 402 [9] A. Mignone, G. Bodo, An HLLC Riemann solver for relativistic flows – II. Magnetohydrodynamics,
403 *Monthly Notices of the Royal Astronomical Society* 368 (3) (2006) 1040–1054. doi:10.1111/J.
404 1365-2966.2006.10162.X.
- 405 [10] S. S. Komissarov, Multidimensional numerical scheme for resistive relativistic magnetohydrody-
406 namics, *Monthly Notices of the Royal Astronomical Society* 382 (3) (2007) 995–1004. doi:
407 10.1111/j.1365-2966.2007.12448.x.
- 408 [11] D. S. Balsara, J. Kim, A subluminal relativistic magnetohydrodynamics scheme with ADER-WENO
409 predictor and multidimensional Riemann solver-based corrector, *Journal of Computational Physics*
410 312 (2016) 357–384. doi:10.1016/j.jcp.2016.02.001.
- 411 [12] T. Amano, A second-order divergence-constrained multidimensional numerical scheme for Rela-
412 tivistic Two-Fluid Electrodynamics, *The Astrophysical Journal* 831 (1) (2016) 100. doi:10.3847/
413 0004-637x/831/1/100.
- 414 [13] U. Shumlak, J. Loverich, Approximate Riemann solver for the two-fluid plasma model, *Journal of*
415 *Computational Physics* 187 (2) (2003) 620–638. doi:10.1016/S0021-9991(03)00151-7.

- 416 [14] A. Hakim, J. Loverich, U. Shumlak, A high resolution wave propagation scheme for ideal Two-Fluid
417 plasma equations, *Journal of Computational Physics* 219 (1) (2006) 418–442. doi:10.1016/j.jcp.
418 2006.03.036.
- 419 [15] H. Kumar, S. Mishra, Entropy stable numerical schemes for two-fluid plasma equations, *Journal of*
420 *Scientific Computing* 52 (2) (2012) 401–425. doi:10.1007/s10915-011-9554-7.
- 421 [16] R. Abgrall, H. Kumar, Robust Finite Volume Schemes for Two-Fluid Plasma Equations, *Journal of*
422 *Scientific Computing* 60 (3) (2014) 584–611. doi:10.1007/s10915-013-9809-6.
- 423 [17] D. M. Bond, V. Wheatley, R. Samtaney, Plasma flow simulation using the two-fluid model, in:
424 *Proceedings of the 20th Australasian Fluid Mechanics Conference*, 2016.
- 425 [18] Y. Li, R. Samtaney, D. Bond, V. Wheatley, Richtmyer-Meshkov instability of an imploding flow
426 with a two-fluid plasma model, *Physical Review Fluids* 5 (11) (2020) 113701. doi:10.1103/
427 PhysRevFluids.5.113701.
- 428 [19] A. K. Meena, H. Kumar, Robust numerical schemes for Two-Fluid Ten-Moment plasma flow equa-
429 tions, *Zeitschrift für Angewandte Mathematik und Physik* 70 (1) (2019) 1–30. doi:10.1007/
430 s00033-018-1061-3.
- 431 [20] S. Zenitani, M. Hesse, A. Klimas, Relativistic two-fluid simulations of guide field magnetic recon-
432 nection, *Astrophysical Journal* 705 (1) (2009) 907–913. doi:10.1088/0004-637X/705/1/907.
- 433 [21] S. Zenitani, M. Hesse, A. Klimas, Resistive magnetohydrodynamic simulations of relativistic
434 magnetic reconnection, *Astrophysical Journal Letters* 716 (2) (2010) L214–L218. doi:10.1088/
435 2041-8205/716/2/L214.
- 436 [22] T. Amano, J. G. Kirk, The role of superluminal electromagnetic waves in pulsar wind termination
437 shocks, *Astrophysical Journal* 770 (1) (2013) 18. doi:10.1088/0004-637X/770/1/18.
- 438 [23] M. Barkov, S. S. Komissarov, V. Korolev, A. Zankovich, A multidimensional numerical scheme for
439 two-fluid relativistic magnetohydrodynamics, *Monthly Notices of the Royal Astronomical Society*
440 438 (1) (2014) 704–716. doi:10.1093/mnras/stt2247.
- 441 [24] M. V. Barkov, S. S. Komissarov, Relativistic tearing and drift-kink instabilities in two-fluid sim-
442 ulations, *Monthly Notices of the Royal Astronomical Society* 458 (2) (2016) 1939–1947. doi:
443 10.1093/mnras/stw384.
- 444 [25] R. J. LeVeque, *Finite Volume Methods for Hyperbolic Problems*, Cambridge University Press, 2002.
445 doi:10.1017/cbo9780511791253.
- 446 [26] E. Chiodaroli, C. De Lellis, O. Kreml, Global Ill-Posedness of the Isentropic System of Gas
447 Dynamics, *Communications on Pure and Applied Mathematics* 68 (7) (2015) 1157–1190. doi:
448 10.1002/CPA.21537.
- 449 [27] E. Godlewski, P.-A. Raviart, *Numerical Approximation of Hyperbolic Systems of Conservation*
450 *Laws*, Vol. 118 of *Applied Mathematical Sciences*, Springer New York, New York, NY, 1996. doi:
451 10.1007/978-1-4612-0713-9.
- 452 [28] S. Zenitani, M. Hesse, A. Klimas, Two-fluid magnetohydrodynamic simulations of relativistic mag-
453 netic reconnection, *Astrophysical Journal* 696 (2) (2009) 1385–1401. doi:10.1088/0004-637X/696/
454 2/1385.
- 455 [29] D. S. Balsara, T. Amano, S. Garain, J. Kim, A high-order relativistic two-fluid electrodynamic
456 scheme with consistent reconstruction of electromagnetic fields and a multidimensional Riemann
457 solver for electromagnetism, *Journal of Computational Physics* 318 (2016) 169–200. doi:10.1016/
458 j.jcp.2016.05.006.
- 459 [30] U. S. Fjordholm, S. Mishra, E. Tadmor, Arbitrarily high-order accurate entropy stable essentially
460 nonoscillatory schemes for systems of conservation laws, *SIAM Journal on Numerical Analysis* 50 (2)
461 (2012) 544–573. doi:10.1137/110836961.

- 462 [31] U. S. Fjordholm, S. Mishra, E. Tadmor, ENO Reconstruction and ENO Interpolation Are
463 Stable, *Foundations of Computational Mathematics* 13 (2) (2013) 139–159. doi:10.1007/
464 s10208-012-9117-9.
- 465 [32] P. Chandrashekar, Kinetic energy preserving and entropy stable finite volume schemes for compress-
466 ible euler and Navier-Stokes equations, *Communications in Computational Physics* 14 (5) (2013)
467 1252–1286. doi:10.4208/cicp.170712.010313a.
- 468 [33] C. Sen, H. Kumar, Entropy Stable Schemes For Ten-Moment Gaussian Closure Equations, *Journal*
469 *of Scientific Computing* 75 (2) (2018) 1128–1155. doi:10.1007/S10915-017-0579-4/FIGURES/8.
- 470 [34] J. Duan, H. Tang, High-order accurate entropy stable finite difference schemes for the shallow water
471 magnetohydrodynamics, *Journal of Computational Physics* 431 (2021) 110136. doi:10.1016/J.
472 JCP.2021.110136.
- 473 [35] J. Duan, H. Tang, High-Order Accurate Entropy Stable Finite Difference Schemes for One- And Two-
474 Dimensional Special Relativistic Hydrodynamics, *Advances in Applied Mathematics and Mechanics*
475 12 (1) (2020) 1–29. doi:10.4208/AAMM.OA-2019-0124.
- 476 [36] B. Biswas, H. Kumar, D. Bhoriya, Entropy stable discontinuous Galerkin schemes for the special
477 relativistic hydrodynamics equations, *Computers & Mathematics with Applications* 112 (September
478 2021) (2022) 55–75. doi:10.1016/j.camwa.2022.02.019.
- 479 [37] C. D. Munz, P. Omnes, R. Schneider, E. Sonnendrücker, U. Voß, Divergence Correction Techniques
480 for Maxwell Solvers Based on a Hyperbolic Model, *Journal of Computational Physics* 161 (2) (2000)
481 484–511. doi:10.1006/jcph.2000.6507.
- 482 [38] V. Schneider, U. Katscher, D. H. Rischke, B. Waldhauser, J. A. Maruhn, C. D. Munz, New Algo-
483 rithms for Ultra-relativistic Numerical Hydrodynamics, *Journal of Computational Physics* 105 (1)
484 (1993) 92–107. doi:10.1006/jcph.1993.1056.
- 485 [39] E. Tadmor, The Numerical Viscosity of Entropy Stable Schemes for Systems of Conservation Laws.
486 I, *Mathematics of Computation* 49 (179) (1987) 91. doi:10.2307/2008251.
- 487 [40] F. Ismail, P. L. Roe, Affordable, entropy-consistent Euler flux functions II: Entropy production at
488 shocks, *Journal of Computational Physics* 228 (15) (2009) 5410–5436. doi:10.1016/j.jcp.2009.
489 04.021.
- 490 [41] P. G. Lefloch, J. M. Mercier, C. Rohde, Fully discrete, entropy conservative schemes of ar-
491 bitrary order, *SIAM Journal on Numerical Analysis* 40 (5) (2002) 1968–1992. doi:10.1137/
492 S003614290240069X.
- 493 [42] T. J. Barth, Numerical methods for gas-dynamics systems on unstructured meshes, An introduction
494 to recent developments in theory and numerics of conservation Laws, Lecture notes in computa-
495 tional science and engineering volume {5}, Springer, Berlin. Eds: D. Kroner, M., Springer, Berlin,
496 Heidelberg, 1999.
- 497 [43] G. S. Jiang, C. W. Shu, Efficient implementation of weighted ENO schemes, *Journal of Computa-*
498 *tional Physics* 126 (1) (1996) 202–228. doi:10.1006/jcph.1996.0130.
- 499 [44] S. Gottlieb, C. W. Shu, E. Tadmor, Strong stability-preserving high-order time discretization meth-
500 ods, *SIAM Review* 43 (1) (2001) 89–112. doi:10.1137/S003614450036757X.
- 501 [45] L. Pareschi, G. Russo, Implicit-explicit Runge-Kutta schemes and applications to hyperbolic sys-
502 tems with relaxation, *Journal of Scientific Computing* 25 (1) (2005) 129–155. doi:10.1007/
503 s10915-004-4636-4.
- 504 [46] J. E. Dennis, R. B. Schnabel, Numerical Methods for Unconstrained Optimization and Nonlinear
505 Equations, Society for Industrial and Applied Mathematics, 1996. doi:10.1137/1.9781611971200.
- 506 [47] C. A. Kennedy, M. H. Carpenter, Additive Runge-Kutta schemes for convection-diffusion-reaction
507 equations, *Applied Numerical Mathematics* 44 (1-2) (2003) 139–181. doi:10.1016/S0168-9274(02)
508 00138-1.

- 509 [48] S. A. Orszag, C. M. Tang, Small-scale structure of two-dimensional magnetohydrodynamic turbu-
510 lence, *Journal of Fluid Mechanics* 90 (1) (1979) 129–143. doi:10.1017/S002211207900210X.
- 511 [49] J. Birn, J. F. Drake, M. A. Shay, B. N. Rogers, R. E. Denton, M. Hesse, M. Kuznetsova, Z. W. Ma,
512 A. Bhattacharjee, A. Otto, P. L. Pritchett, *Geospace Environmental Modeling (GEM) Magnetic*
513 *Reconnection Challenge, Journal of Geophysical Research: Space Physics* 106 (A3) (2001) 3715–
514 3719. doi:10.1029/1999ja900449.

515 A Proof of Proposition 3.1

516 We will give the proof of Proposition (3.1) in two steps. Firstly, we will prove two lemmas, and then we
517 give the proof of proposition using these two lemmas. The proof is similar to those in [1] for relativistic
518 hydrodynamics except for the additional source terms and three-dimensional velocity field.

Lemma A.1. *The smooth solutions of the system (4) satisfies the following identity*

$$\frac{1}{\Gamma_\alpha^2} \partial_t p_\alpha = \partial_t p_\alpha + u_{x_\alpha} \partial_x p_\alpha + \left(\frac{\rho_\alpha h_\alpha}{\Gamma_\alpha} \right) (\partial_t \Gamma_\alpha + \partial_x (\Gamma_\alpha u_{x_\alpha})) - \rho_\alpha h_\alpha \partial_x u_{x_\alpha} - \mathbf{u}_\alpha \cdot (\mathbf{s}_{M_\alpha} - \mathbf{u}_\alpha \mathbf{s}_{\mathcal{E}_\alpha}), \quad (34)$$

where

$$\mathbf{s}_{M_\alpha} = r_\alpha \Gamma_\alpha \rho_\alpha (\mathbf{E} + \mathbf{u}_\alpha \times \mathbf{B}), \quad \mathbf{s}_{\mathcal{E}_\alpha} = r_\alpha \Gamma_\alpha \rho_\alpha (\mathbf{u}_\alpha \cdot \mathbf{E}).$$

519 are the source terms in the momentum and energy equations.

Proof. Let \mathbf{U} be the smooth solution of the system (4). Then we can write,

$$\partial_t (\rho_\alpha \Gamma_\alpha) + \partial_x (\rho_\alpha \Gamma_\alpha u_{x_\alpha}) = 0, \quad (35)$$

$$\partial_t (\rho_\alpha h_\alpha \Gamma_\alpha^2 u_{x_\alpha}) + \partial_x (\rho_\alpha h_\alpha \Gamma_\alpha^2 u_{x_\alpha}^2) + \partial_x p_\alpha = \mathbf{s}_{M_{x_\alpha}}, \quad (36)$$

$$\partial_t (\rho_\alpha h_\alpha \Gamma_\alpha^2 u_{y_\alpha}) + \partial_x (\rho_\alpha h_\alpha \Gamma_\alpha^2 u_{x_\alpha} u_{y_\alpha}) = \mathbf{s}_{M_{y_\alpha}}, \quad (37)$$

$$\partial_t (\rho_\alpha h_\alpha \Gamma_\alpha^2 u_{z_\alpha}) + \partial_x (\rho_\alpha h_\alpha \Gamma_\alpha^2 u_{x_\alpha} u_{z_\alpha}) = \mathbf{s}_{M_{z_\alpha}}, \quad (38)$$

$$\partial_t (\rho_\alpha h_\alpha \Gamma_\alpha^2) - \partial_t p_\alpha + \partial_x (\rho_\alpha h_\alpha \Gamma_\alpha^2 u_{x_\alpha}) = \mathbf{s}_{\mathcal{E}_\alpha}, \quad (39)$$

where, we have used $\mathbf{s}_{M_\alpha} = (\mathbf{s}_{M_{x_\alpha}}, \mathbf{s}_{M_{y_\alpha}}, \mathbf{s}_{M_{z_\alpha}})$, as the momentum source vector, i.e., source terms of the Eqns. (1b) and (1e). Also, $\mathbf{s}_{\mathcal{E}_\alpha}$ is the source term of the energy equations (1c), and (1f). We apply the product rule on Equations (36)-(38) and substitute the value of $\partial_x (\rho_\alpha h_\alpha \Gamma_\alpha^2 u_{x_\alpha})$ from Eqn. (39) in each of the three equations to obtain the following set of three identities:

$$(\rho_\alpha h_\alpha \Gamma_\alpha^2 u_{x_\alpha}) (\partial_t u_{x_\alpha} + u_{x_\alpha} \partial_x u_{x_\alpha}) + u_{x_\alpha}^2 \partial_t p_\alpha + u_{x_\alpha} \partial_x p_\alpha = u_{x_\alpha} (\mathbf{s}_{M_{x_\alpha}} - u_{x_\alpha} \mathbf{s}_{\mathcal{E}_\alpha}) \quad (40a)$$

$$(\rho_\alpha h_\alpha \Gamma_\alpha^2 u_{y_\alpha}) (\partial_t u_{y_\alpha} + u_{y_\alpha} \partial_x u_{y_\alpha}) + u_{y_\alpha}^2 \partial_t p_\alpha = u_{y_\alpha} (\mathbf{s}_{M_{y_\alpha}} - u_{y_\alpha} \mathbf{s}_{\mathcal{E}_\alpha}) \quad (40b)$$

$$(\rho_\alpha h_\alpha \Gamma_\alpha^2 u_{z_\alpha}) (\partial_t u_{z_\alpha} + u_{z_\alpha} \partial_x u_{z_\alpha}) + u_{z_\alpha}^2 \partial_t p_\alpha = u_{z_\alpha} (\mathbf{s}_{M_{z_\alpha}} - u_{z_\alpha} \mathbf{s}_{\mathcal{E}_\alpha}) \quad (40c)$$

We observe that $\partial_t \Gamma_\alpha = \Gamma_\alpha^3 \mathbf{u}_\alpha \cdot \partial_t \mathbf{u}_\alpha$, and $\partial_x \Gamma_\alpha = \Gamma_\alpha^3 \mathbf{u}_\alpha \cdot \partial_x \mathbf{u}_\alpha$. Consequently, Eqn. (40a) simplifies to

$$\begin{aligned} & \left(\frac{\rho_\alpha h_\alpha}{\Gamma_\alpha} \right) (\partial_t \Gamma_\alpha + u_{x_\alpha} \partial_x \Gamma_\alpha) - \rho_\alpha h_\alpha \Gamma_\alpha^2 u_{y_\alpha} (\partial_t u_{y_\alpha} + u_{x_\alpha} \partial_x u_{y_\alpha}) - \rho_\alpha h_\alpha \Gamma_\alpha^2 u_{z_\alpha} (\partial_t u_{z_\alpha} + u_{x_\alpha} \partial_x u_{z_\alpha}) \\ & + u_{x_\alpha}^2 \partial_t p_\alpha + u_{x_\alpha} \partial_x p_\alpha = u_{x_\alpha} (\mathbf{s}_{M_{x_\alpha}} - u_{x_\alpha} \mathbf{s}_{\mathcal{E}_\alpha}), \end{aligned} \quad (41)$$

520 From the definition of Lorentz factor Γ_α , we have $u_{x_\alpha}^2 = 1 - \frac{1}{\Gamma_\alpha^2} - u_{y_\alpha}^2 - u_{z_\alpha}^2$. We substitute this value of
521 $u_{x_\alpha}^2$ in Eqn. (41), followed by the substitution of value of $u_{y_\alpha}^2 \partial_t p_\alpha$ and $u_{z_\alpha}^2 \partial_t p_\alpha$ from the Eqn. (40b)-(40c),
522 to obtain the required identity (34). \square

Lemma A.2. *For smooth solutions of the system (4), we have the following identity*

$$(\partial_t p_\alpha + u_{x_\alpha} \partial_x p_\alpha) + \frac{p_\alpha \gamma_\alpha}{\Gamma_\alpha} (\partial_t \Gamma_\alpha + \partial_x (\Gamma_\alpha u_{x_\alpha})) = 0. \quad (42)$$

Proof. We expand Eqn. (39) using the product rule and simplify further using the substitution of variables from Eqn. (35) to obtain,

$$\begin{aligned} \partial_t p_\alpha + u_{x_\alpha} \partial_x p_\alpha &= \left(\frac{\gamma_\alpha - 1}{\Gamma_\alpha^2 \gamma_\alpha} \right) \mathbf{s} \varepsilon_\alpha + \left(\frac{\gamma_\alpha - 1}{\Gamma_\alpha^2 \gamma_\alpha} \right) \partial_t p_\alpha - \left(\frac{\rho_\alpha \gamma_\alpha - 1}{\Gamma_\alpha \gamma_\alpha} \right) (\partial_t \Gamma_\alpha + \partial_x (\Gamma_\alpha u_{x_\alpha})) \\ &\quad - 2(\partial_t \Gamma_\alpha + \partial_x (\Gamma_\alpha u_{x_\alpha})) \frac{p_\alpha}{\Gamma_\alpha} + \rho_\alpha \left(\frac{\gamma_\alpha - 1}{\gamma_\alpha} \right) \partial_x u_{x_\alpha} + p_\alpha \partial_x u_{x_\alpha}. \end{aligned} \quad (43)$$

Substituting the value of $\frac{1}{\Gamma_\alpha^2} \partial_t p_\alpha$ from the identity of Lemma (A.1), and simplifying further we get

$$\begin{aligned} \partial_t p_\alpha + u_{x_\alpha} \partial_x p_\alpha &= \left(\frac{\gamma_\alpha - 1}{\gamma_\alpha} \right) \left(-\mathbf{u}_\alpha \cdot \mathbf{s} \mathbf{M}_\alpha + \left(\frac{1 + \mathbf{u}_\alpha^2}{\Gamma_\alpha^2} \right) \mathbf{s} \varepsilon_\alpha \right) \\ &\quad + \left(\frac{\gamma_\alpha - 1}{\gamma_\alpha} \right) (\partial_t p_\alpha + u_{x_\alpha} \partial_x p_\alpha) \\ &\quad + \left(\frac{\gamma_\alpha - 1}{\gamma_\alpha} \right) \left[\left(\frac{\rho_\alpha h_\alpha}{\Gamma_\alpha} \right) (\partial_t \Gamma_\alpha + \partial_x (\Gamma_\alpha u_{x_\alpha})) - \rho_\alpha h_\alpha \partial_x u_{x_\alpha} \right] \\ &\quad - \left(\frac{\rho_\alpha \gamma_\alpha - 1}{\Gamma_\alpha \gamma_\alpha} \right) (\partial_t \Gamma_\alpha + \partial_x (\Gamma_\alpha u_{x_\alpha})) - \frac{2p_\alpha}{\Gamma_\alpha} (\partial_t \Gamma_\alpha + \partial_x (\Gamma_\alpha u_{x_\alpha})) \\ &\quad + \left(\frac{\gamma_\alpha - 1}{\gamma_\alpha} \right) \rho_\alpha \partial_x u_{x_\alpha} + p_\alpha \partial_x u_{x_\alpha}, \end{aligned}$$

523 We observe that $\mathbf{u}_\alpha \cdot \mathbf{s} \mathbf{M}_\alpha - \mathbf{s} \varepsilon_\alpha = 0$, thus, after further simplifications and cancellations [1], we obtain (42).
524 □

Proof of Proposition (3.1). We find the partial derivatives of $s_\alpha = \ln(p_\alpha \rho_\alpha^{-\gamma_\alpha})$ with respect to t and x , to obtain

$$\partial_t s_\alpha = \frac{1}{p_\alpha} \partial_t p_\alpha - \frac{\gamma_\alpha}{\rho_\alpha} \partial_t \rho_\alpha \quad \text{and} \quad \partial_x s_\alpha = \frac{1}{p_\alpha} \partial_x p_\alpha - \frac{\gamma_\alpha}{\rho_\alpha} \partial_x \rho_\alpha. \quad (44)$$

Applying the product rule on the mass density Eqn. (35) we obtain an identity in terms of the partial derivatives of ρ_α

$$\frac{1}{\rho_\alpha} (\partial_t \rho_\alpha + u_{x_\alpha} \partial_x \rho_\alpha) = -\frac{1}{\Gamma_\alpha} (\partial_t \Gamma_\alpha + \partial_x (\Gamma_\alpha u_{x_\alpha})). \quad (45)$$

Combining Eqn. (42) and Eqn. (45), we obtain the expression

$$\frac{1}{p_\alpha} (\partial_t p_\alpha + u_{x_\alpha} \partial_x p_\alpha) - \frac{\gamma_\alpha}{\rho_\alpha} (\partial_t \rho_\alpha + u_{x_\alpha} \partial_x \rho_\alpha) = 0,$$

525 which, on using Eqn. (44), is equivalent to $\partial_t s_\alpha + u_{x_\alpha} \partial_x s_\alpha = 0$. The identity (5) is a direct consequence
526 of the product rule. To obtain the final entropy equality (6), we simplify the identity (5) by choosing
527 particular value of $H(s_\alpha)$ as $H(s_\alpha) = \frac{-s_\alpha}{\gamma_\alpha - 1}$. □

528

529 B Barth scaling of right eigenvectors

530 Here, we present expressions for the right eigenvectors and scaled right eigenvectors for the conservative
531 system (3). The right eigenvectors are described in Section B.1, while the expressions and procedure to
532 obtain the scaled eigenvectors is presented in Section B.2

533 B.1 Right eigenvectors

The set of right eigenvectors of the matrix $\mathbf{A}^x = \frac{\partial \mathbf{f}^x}{\partial \mathbf{U}}$ corresponding to the eigenvalues Λ^x of the system (3) is obtained by taking $d = x$ in the ordered set $\mathbf{R}_{\Lambda^d}^d = \{(\mathbf{R}_{\Lambda^d}^d)_n : n = 1, 2, 3, \dots, 18\}$ where the vectors $(\mathbf{R}_{\Lambda^d}^d)_n$ are defined as

$$(\mathbf{R}_{\Lambda^d}^d)_n = \begin{cases} \left((\mathbf{R}_{i,k}^d)_{1 \times 5}, \mathbf{0}_{1 \times 5}, \mathbf{0}_{1 \times 8} \right)^\top, & 1 \leq n \leq 5, k = n \\ \left(\mathbf{0}_{1 \times 5}, (\mathbf{R}_{e,k}^d)_{1 \times 5}, \mathbf{0}_{1 \times 8} \right)^\top, & 6 \leq n \leq 10, k = n - 5 \\ \left(\mathbf{0}_{1 \times 5}, \mathbf{0}_{1 \times 5}, (\mathbf{R}_{m,k}^d)_{1 \times 8} \right)^\top, & 11 \leq n \leq 18, k = n - 10, \end{cases} \quad (46)$$

534 where $\mathbf{R}_{\alpha,k}^d$, $\alpha \in \{i, e\}$, is the k^{th} column vector of the 5×5 right eigenvector matrices \mathbf{R}_α^d of the
535 flux jacobians $\frac{\partial \mathbf{f}_\alpha^d}{\partial \mathbf{U}_\alpha}$, and $\mathbf{R}_{m,k}^d$ is the k^{th} column vector of the right eigenvector matrix \mathbf{R}_m^d of the flux
536 jacobian matrix $\frac{\partial \mathbf{f}_m^d}{\partial \mathbf{U}_m}$. The matrices \mathbf{R}_α^k and \mathbf{R}_m^k have the following expressions.

- For $d = x, y$, and $\alpha \in \{i, e\}$, the right eigenvector matrix \mathbf{R}_α^d is given by the relation,

$$\mathbf{R}_\alpha^d = \left(\frac{\partial \mathbf{U}_\alpha}{\partial \mathbf{W}_\alpha} \right) \mathbf{R}_{\alpha, \mathbf{W}}, \quad (47)$$

where the matrix $\mathbf{R}_{\alpha, \mathbf{W}}^d$ for $d = x$ is given by,

$$\mathbf{R}_{\alpha, \mathbf{W}}^x = \begin{pmatrix} \frac{1}{c_\alpha^2 h_\alpha} & 1 & 0 & 0 & \frac{1}{c_\alpha^2 h_\alpha} \\ -\frac{\sqrt{Q_\alpha^x}}{c_\alpha h_\alpha \Gamma_\alpha \rho_\alpha} & 0 & 0 & 0 & \frac{\sqrt{Q_\alpha^x}}{c_\alpha h_\alpha \Gamma_\alpha \rho_\alpha} \\ \frac{(c_\alpha - \Gamma_\alpha \sqrt{Q_\alpha^x} u_{x\alpha}) u_{y\alpha}}{c_\alpha h_\alpha \Gamma_\alpha^2 \rho_\alpha (u_{x\alpha}^2 - 1)} & 0 & 1 & 0 & \frac{(c_\alpha + \Gamma_\alpha \sqrt{Q_\alpha^x} u_{x\alpha}) u_{y\alpha}}{c_\alpha h_\alpha \Gamma_\alpha^2 \rho_\alpha (u_{x\alpha}^2 - 1)} \\ \frac{(c_\alpha - \Gamma_\alpha \sqrt{Q_\alpha^x} u_{x\alpha}) u_{z\alpha}}{c_\alpha h_\alpha \Gamma_\alpha^2 \rho_\alpha (u_{x\alpha}^2 - 1)} & 0 & 0 & 1 & \frac{(c_\alpha + \Gamma_\alpha \sqrt{Q_\alpha^x} u_{x\alpha}) u_{z\alpha}}{c_\alpha h_\alpha \Gamma_\alpha^2 \rho_\alpha (u_{x\alpha}^2 - 1)} \\ 1 & 0 & 0 & 0 & 1 \end{pmatrix}. \quad (48)$$

- The eigenvector matrix \mathbf{R}_m^d for $d = x$ is given by,

$$\mathbf{R}_m^x = \begin{pmatrix} 0 & -1 & 0 & 0 & 0 & 0 & 1 & 0 \\ 0 & 0 & 0 & 1 & 0 & -1 & 0 & 0 \\ 0 & 0 & -1 & 0 & 1 & 0 & 0 & 0 \\ -1 & 0 & 0 & 0 & 0 & 0 & 0 & 1 \\ 0 & 0 & 1 & 0 & 1 & 0 & 0 & 0 \\ 0 & 0 & 0 & 1 & 0 & 1 & 0 & 0 \\ 1 & 0 & 0 & 0 & 0 & 0 & 0 & 1 \\ 0 & 1 & 0 & 0 & 0 & 0 & 1 & 0 \end{pmatrix}.$$

Remark B.1. For the y -directional flux, \mathbf{f}^y , we proceed similarly to get the set of eigenvalues Λ^y of the jacobian matrix $\frac{\partial \mathbf{f}^y}{\partial \mathbf{U}}$ as,

$$\Lambda^y = \left\{ \frac{(1 - c_i^2) u_{y_i} - (c_i / \Gamma_i) \sqrt{Q_i^y}}{1 - c_i^2 |\mathbf{u}_i|^2}, u_{y_i}, u_{y_i}, u_{y_i}, \frac{(1 - c_i^2) u_{y_i} + (c_i / \Gamma_i) \sqrt{Q_i^y}}{1 - c_i^2 |\mathbf{u}_i|^2}, \right. \\ \left. \frac{(1 - c_e^2) u_{y_e} - (c_e / \Gamma_e) \sqrt{Q_e^y}}{1 - c_e^2 |\mathbf{u}_e|^2}, u_{y_e}, u_{y_e}, u_{y_e}, \frac{(1 - c_e^2) u_{y_e} + (c_e / \Gamma_e) \sqrt{Q_e^y}}{1 - c_e^2 |\mathbf{u}_e|^2}, \right. \\ \left. -\chi, -\kappa, -1, -1, 1, 1, \kappa, \chi \right\},$$

where, $Q_\alpha^y = 1 - u_{y_\alpha}^2 - c_\alpha^2(u_{x_\alpha}^2 + u_{z_\alpha}^2)$, $\alpha \in \{i, e\}$. The corresponding right eigenvectors are given by fixing $d = y$ in the ordered set $\mathbf{R}_{\Lambda^d}^d = \{(\mathbf{R}_{\Lambda^d}^d)_n : n = 1, 2, 3, \dots, 18\}$ where $(\mathbf{R}_{\Lambda^d}^d)_n$ is defined by Eqn. (46) and the updated y -directional matrices $\mathbf{R}_{\alpha, \mathbf{W}}^y$ and \mathbf{R}_m^y are given by

$$\mathbf{R}_{\alpha, \mathbf{W}}^y = \begin{pmatrix} \frac{1}{c_\alpha^2 h_\alpha} & 1 & 0 & 0 & \frac{1}{c_\alpha^2 h_\alpha} \\ \frac{(c_\alpha - \Gamma_\alpha \sqrt{Q_\alpha^y} u_{y_\alpha}) u_{x_\alpha}}{c_\alpha h_\alpha \Gamma_\alpha^2 \rho_\alpha (u_{y_\alpha}^2 - 1)} & 0 & 1 & 0 & \frac{(c_\alpha + \Gamma_\alpha \sqrt{Q_\alpha^y} u_{y_\alpha}) u_{x_\alpha}}{c_\alpha h_\alpha \Gamma_\alpha^2 \rho_\alpha (u_{y_\alpha}^2 - 1)} \\ -\sqrt{Q_\alpha^y} & 0 & 0 & 0 & +\sqrt{Q_\alpha^y} \\ \frac{c_\alpha h_\alpha \Gamma_\alpha \rho_\alpha}{c_\alpha h_\alpha \Gamma_\alpha \rho_\alpha} & 0 & 0 & 0 & \frac{c_\alpha h_\alpha \Gamma_\alpha \rho_\alpha}{c_\alpha h_\alpha \Gamma_\alpha \rho_\alpha} \\ \frac{(c_\alpha - \Gamma_\alpha \sqrt{Q_\alpha^y} u_{y_\alpha}) u_{z_\alpha}}{c_\alpha h_\alpha \Gamma_\alpha^2 \rho_\alpha (u_{y_\alpha}^2 - 1)} & 0 & 0 & 1 & \frac{(c_\alpha + \Gamma_\alpha \sqrt{Q_\alpha^y} u_{y_\alpha}) u_{z_\alpha}}{c_\alpha h_\alpha \Gamma_\alpha^2 \rho_\alpha (u_{y_\alpha}^2 - 1)} \\ 1 & 0 & 0 & 0 & 1 \end{pmatrix}, \quad (49)$$

$$\mathbf{R}_m^y = \begin{pmatrix} 0 & 0 & 0 & -1 & 0 & 1 & 0 & 0 \\ 0 & -1 & 0 & 0 & 0 & 0 & 1 & 0 \\ 0 & 0 & 1 & 0 & -1 & 0 & 0 & 0 \\ 0 & 0 & 1 & 0 & 1 & 0 & 0 & 0 \\ -1 & 0 & 0 & 0 & 0 & 0 & 0 & 1 \\ 0 & 0 & 0 & 1 & 0 & 1 & 0 & 0 \\ 1 & 0 & 0 & 0 & 0 & 0 & 0 & 1 \\ 0 & 1 & 0 & 0 & 0 & 0 & 1 & 0 \end{pmatrix}. \quad (50)$$

537 B.2 Barth scaling and entropy scaled right eigenvectors

538 We ignore the superscript x to derive the entropy scaled right eigenvectors for the x -directional part; for
539 the y -directional flux, we proceed similarly. We have the entropy variable vector \mathbf{V}_α as

$$\mathbf{V}_\alpha = \begin{pmatrix} \frac{\gamma_\alpha - s_\alpha}{\gamma_\alpha - 1} + \beta_\alpha \\ u_{x_\alpha} \Gamma_\alpha \beta_\alpha \\ u_{y_\alpha} \Gamma_\alpha \beta_\alpha \\ u_{z_\alpha} \Gamma_\alpha \beta_\alpha \\ -\Gamma_\alpha \beta_\alpha \end{pmatrix}, \quad \text{where } \beta_\alpha = \frac{\rho_\alpha}{p_\alpha}.$$

We want to find scaling matrices \mathbf{T}_α^d ($d \in \{x, y\}$ and $\alpha \in \{i, e\}$) such that the scaled right eigenvector matrices $\tilde{\mathbf{R}}_\alpha^d = \mathbf{R}_\alpha^d \mathbf{T}_\alpha^d$, with \mathbf{R}_α^d as in Eqn. (47), satisfy

$$\frac{\partial \mathbf{U}_\alpha}{\partial \mathbf{V}_\alpha} = \tilde{\mathbf{R}}_\alpha^d (\tilde{\mathbf{R}}_\alpha^d)^\top.$$

The matrices \mathbf{T}_α^d are known as Barth scaling matrices. Following the procedure of [42], the scaling matrices \mathbf{T}_α^d are given by the square root of the matrices \mathbf{Y}_α^d where the expression for matrices \mathbf{Y}_α^d is given by the formulae

$$\mathbf{Y}_\alpha^d = (\mathbf{R}_{\alpha, \mathbf{W}}^d)^{-1} \frac{\partial \mathbf{W}_\alpha}{\partial \mathbf{V}_\alpha} \frac{\partial \mathbf{U}_\alpha}{\partial \mathbf{W}_\alpha}^{-\top} \mathbf{R}_{\alpha, \mathbf{W}}^d^{-\top},$$

where the matrices $\mathbf{R}_{\alpha, \mathbf{W}}^d$ are given by Eqn. (48) for $d = x$, and for the case $d = y$ the expressions for the matrices follows from Eqn. (49). Assuming $d = x$ for the clarity. A long simplification leads to the expressions

$$\mathbf{Y}_\alpha^x = \begin{pmatrix} \frac{c_\alpha^2 h_\alpha p_\alpha \left(1 + \frac{c_\alpha u_{x_\alpha}}{\Gamma_\alpha \sqrt{Q_\alpha^x}}\right)}{2\Gamma_\alpha (1 - c_\alpha^2 |\mathbf{u}_\alpha^x|^2)} & 0 & 0 & 0 & 0 \\ 0 & \frac{\rho_\alpha}{\Gamma_\alpha} \frac{\gamma_\alpha - 1}{\gamma_\alpha} & 0 & 0 & 0 \\ 0 & 0 & Y_{\alpha 33}^x & Y_{\alpha 34}^x & 0 \\ 0 & 0 & Y_{\alpha 43}^x & Y_{\alpha 44}^x & 0 \\ 0 & 0 & 0 & 0 & \frac{c_\alpha^2 h_\alpha p_\alpha \left(1 - \frac{c_\alpha u_{x_\alpha}}{\Gamma_\alpha \sqrt{Q_\alpha^x}}\right)}{2\Gamma_\alpha (1 - c_\alpha^2 |\mathbf{u}_\alpha^x|^2)} \end{pmatrix}$$

where, $Q_\alpha^x = 1 - u_{x_\alpha}^2 - c_\alpha^2(u_{y_\alpha}^2 + u_{z_\alpha}^2)$, $Y_{\alpha 33}^x = C_\alpha^x(1 - u_{x_\alpha}^2 - u_{y_\alpha}^2)$, $Y_{\alpha 44}^x = C_\alpha^x(1 - u_{x_\alpha}^2 - u_{z_\alpha}^2)$, $Y_{\alpha 34}^x = Y_{\alpha 43}^x = -C_\alpha^x u_{y_\alpha} u_{z_\alpha}$ and

$$C_\alpha^x = \frac{p_\alpha}{h_\alpha \Gamma_\alpha^3 \rho_\alpha^2 (1 - u_{x_\alpha}^2)}.$$

Consequently, the matrix $\mathbf{T}_\alpha^x = \sqrt{\mathbf{Y}_\alpha^x}$ is given by

$$\mathbf{T}_\alpha^x = \begin{pmatrix} \sqrt{\frac{c_\alpha^2 h_\alpha p_\alpha \left(1 + \frac{c_\alpha u_{x_\alpha}}{\Gamma_\alpha \sqrt{Q_\alpha^x}}\right)}{2\Gamma_\alpha (1 - c_\alpha^2 |\mathbf{u}_\alpha^2|)}} & 0 & 0 & 0 & 0 \\ 0 & \sqrt{\frac{\rho_\alpha \gamma_\alpha - 1}{\Gamma_\alpha \gamma_\alpha}} & 0 & 0 & 0 \\ 0 & 0 & T_{\alpha 33}^x & T_{\alpha 34}^x & 0 \\ 0 & 0 & T_{\alpha 43}^x & T_{\alpha 44}^x & 0 \\ 0 & 0 & 0 & 0 & \sqrt{\frac{c_\alpha^2 h_\alpha p_\alpha \left(1 - \frac{c_\alpha u_{x_\alpha}}{\Gamma_\alpha \sqrt{Q_\alpha^x}}\right)}{2\Gamma_\alpha (1 - c_\alpha^2 |\mathbf{u}_\alpha^2|)}} \end{pmatrix}$$

where,

$$\begin{pmatrix} T_{\alpha 33}^x & T_{\alpha 34}^x \\ T_{\alpha 43}^x & T_{\alpha 44}^x \end{pmatrix} = \begin{cases} \begin{pmatrix} \sqrt{Y_{\alpha 33}^x} & 0 \\ 0 & \sqrt{Y_{\alpha 44}^x} \end{pmatrix} & \text{if } u_{y_\alpha} = u_{z_\alpha} = 0, \\ \sqrt{C_\alpha^x} \begin{pmatrix} \frac{u_{z_\alpha} \sqrt{1 - u_{x_\alpha}^2} + \frac{u_{y_\alpha}^2}{\Gamma_\alpha}}{u_{y_\alpha}^2 + u_{z_\alpha}^2} & \frac{u_{y_\alpha} u_{z_\alpha}}{u_{y_\alpha}^2 + u_{z_\alpha}^2} \left(\frac{1}{\Gamma_\alpha} - \sqrt{1 - u_{x_\alpha}^2}\right) \\ \frac{u_{y_\alpha} u_{z_\alpha}}{u_{y_\alpha}^2 + u_{z_\alpha}^2} \left(\frac{1}{\Gamma_\alpha} - \sqrt{1 - u_{x_\alpha}^2}\right) & \frac{u_{y_\alpha} \sqrt{1 - u_{x_\alpha}^2} + \frac{u_{z_\alpha}^2}{\Gamma_\alpha}}{u_{y_\alpha}^2 + u_{z_\alpha}^2} \end{pmatrix} & \text{otherwise.} \end{cases}$$

Remark B.2. Proceeding similarly in the y -direction with the matrix $\mathbf{R}_{\alpha, \mathbf{W}}^y$ as in Eqn. (49), the scaling matrix is given by

$$\mathbf{T}_\alpha^y = \begin{pmatrix} \sqrt{\frac{c_\alpha^2 h_\alpha p_\alpha \left(1 + \frac{c_\alpha u_{y_\alpha}}{\Gamma_\alpha \sqrt{Q_\alpha^y}}\right)}{2\Gamma_\alpha (1 - c_\alpha^2 |\mathbf{u}_\alpha^2|)}} & 0 & 0 & 0 & 0 \\ 0 & \sqrt{\frac{\rho_\alpha \gamma_\alpha - 1}{\Gamma_\alpha \gamma_\alpha}} & 0 & 0 & 0 \\ 0 & 0 & T_{\alpha 33}^y & T_{\alpha 34}^y & 0 \\ 0 & 0 & T_{\alpha 43}^y & T_{\alpha 44}^y & 0 \\ 0 & 0 & 0 & 0 & \sqrt{\frac{c_\alpha^2 h_\alpha p_\alpha \left(1 - \frac{c_\alpha u_{y_\alpha}}{\Gamma_\alpha \sqrt{Q_\alpha^y}}\right)}{2\Gamma_\alpha (1 - c_\alpha^2 |\mathbf{u}_\alpha^2|)}} \end{pmatrix}$$

where, $Q_\alpha^y = 1 - u_{y_\alpha}^2 - c_\alpha^2(u_{x_\alpha}^2 + u_{z_\alpha}^2)$, and the block entries are given by the matrices

$$\begin{pmatrix} T_{\alpha 33}^y & T_{\alpha 34}^y \\ T_{\alpha 43}^y & T_{\alpha 44}^y \end{pmatrix} = \begin{cases} \begin{pmatrix} \sqrt{Y_{\alpha 33}^y} & 0 \\ 0 & \sqrt{Y_{\alpha 44}^y} \end{pmatrix} & \text{if } u_{x_\alpha} = u_{z_\alpha} = 0, \\ \sqrt{C_\alpha^y} \begin{pmatrix} \frac{u_{z_\alpha} \sqrt{1 - u_{y_\alpha}^2} + \frac{u_{x_\alpha}^2}{\Gamma_\alpha}}{u_{x_\alpha}^2 + u_{z_\alpha}^2} & \frac{u_{x_\alpha} u_{z_\alpha}}{u_{x_\alpha}^2 + u_{z_\alpha}^2} \left(\frac{1}{\Gamma_\alpha} - \sqrt{1 - u_{y_\alpha}^2}\right) \\ \frac{u_{x_\alpha} u_{z_\alpha}}{u_{x_\alpha}^2 + u_{z_\alpha}^2} \left(\frac{1}{\Gamma_\alpha} - \sqrt{1 - u_{y_\alpha}^2}\right) & \frac{u_{x_\alpha} \sqrt{1 - u_{y_\alpha}^2} + \frac{u_{z_\alpha}^2}{\Gamma_\alpha}}{u_{x_\alpha}^2 + u_{z_\alpha}^2} \end{pmatrix} & \text{otherwise,} \end{cases}$$

with $Y_{\alpha 33}^y = C_\alpha^y(1 - u_{y_\alpha}^2 - u_{x_\alpha}^2)$, $Y_{\alpha 44}^y = C_\alpha^y(1 - u_{y_\alpha}^2 - u_{z_\alpha}^2)$ and

$$C_\alpha^y = \frac{p_\alpha}{h_\alpha \Gamma_\alpha^3 \rho_\alpha^2 (1 - u_{y_\alpha}^2)}.$$

C ARK3-IMEX coefficients table

The coefficients for the third order ARK-IMEX time update are given as follows,

	$l = 0$	$l = 1$	$l = 2$	$l = 3$
$m = 1$	$\frac{1767732205903}{2027836641118}$	0	0	0
$a_{ml}^{[NS]}$				
$m = 2$	$\frac{5535828885825}{10492691773637}$	$\frac{788022342437}{10882634858940}$	0	0
$m = 3$	$\frac{6485989280629}{16251701735622}$	$-\frac{4246266847089}{9704473918619}$	$\frac{10755448449292}{10357097424841}$	0
$m = 1$	$\frac{1767732205903}{405673282236}$	$\frac{1767732205903}{405673282236}$	0	0
$a_{ml}^{[S]}$				
$m = 2$	$\frac{2746238789719}{10658868560708}$	$-\frac{640167445237}{6845629431997}$	$\frac{1767732205903}{405673282236}$	0
$m = 3$	$\frac{1471266399579}{7840856788654}$	$-\frac{4482444167858}{7529755066697}$	$\frac{11266239266428}{11593286722821}$	$\frac{1767732205903}{405673282236}$
$b_l^{[NS]}$	$\frac{1471266399579}{7840856788654}$	$-\frac{4482444167858}{7529755066697}$	$\frac{11266239266428}{11593286722821}$	$\frac{1767732205903}{405673282236}$
$b_l^{[S]}$	$\frac{2756255671327}{12835298489170}$	$-\frac{10771552573575}{22201958757719}$	$\frac{9247589265047}{10645013368117}$	$\frac{2193209047091}{5459859503100}$
c_l	0	$\frac{1767732205903}{2027836641118}$	$\frac{3}{5}$	1

Table 5: The coefficients for ARK3-IMEX time update scheme.